

Article

In Situ U—Pb Dating and Trace Element Analysis of Garnet in the Tongshanling Cu Polymetallic Deposit, South China

Fucheng Tan , Hua Kong ^{*}, Biao Liu, Qianhong Wu and Shefa Chen

Key Laboratory of Metallogenic Prediction of Nonferrous Metals and Geological Environment Monitoring, Ministry of Education, School of Geosciences and Info-Physics, Central South University, Changsha 410083, China
^{*} Correspondence: konghua@csu.edu.cn

Abstract: The grossular–andradite garnet is an ideal mineral for indicating the formation age of skarn, which also pretends to constrain skarn processes because of its higher REE (rare earth elements) content. The Tongshanling deposit is a medium-sized reduced skarn Cu–W–Pb–Zn deposit associated with a highly evolved I-type granodiorite intrusion in the Nanling metallogenic belt, South China. Different mineral assemblages, microscopic characteristics, and BSE images distinguish two kinds of garnets in the prograde and retrograde skarn stages. The garnet grains from the prograde skarn stage have a U–Pb isochron age of 165.4 ± 3.8 Ma (MSWD = 0.7) and that from the retrograde skarn stage have a U–Pb isochron age of 159.5 ± 1.7 Ma (MSWD = 1.8), implying that the thermal metamorphism and hydrothermal metasomatism mainly occurred in the middle Upper Jurassic. The total amount of rare earth elements ($\Sigma\text{REE}+\text{Y}$) in the garnet gradually decreased and the REE patterns shifted from enriched HREE with Eu negative anomaly to HREE-depleted with Eu positive anomaly. The decreasing U content and increasing Eu anomaly in the retrograde skarn stage indicate a redox environment change from oxidation to reduction. However, garnet from different elevations within the same stage (+90 m, +5 m, –35 m, –200 m, and –400 m) exhibit similar REE patterns, despite weak cooling and significant depressurization processes confirmed by fluid inclusion microthermography. As a result, the REE content and patterns are dominated by the REE species of parent fluids, which are changed over time by symbiotic REE-enriched mineral precipitation and the redox environment, while being slightly affected by the fluid pressure. Grossular garnets, rich in U and REEs, and found in reduced skarn deposits, can constrain chronology and reveal the spatio-temporal zonal characteristics.

Keywords: garnet; REE patterns; U–Pb dating; skarn zoning; Tongshanling



Citation: Tan, F.; Kong, H.; Liu, B.; Wu, Q.; Chen, S. In Situ U—Pb Dating and Trace Element Analysis of Garnet in the Tongshanling Cu Polymetallic Deposit, South China. *Minerals* **2023**, *13*, 187. <https://doi.org/10.3390/min13020187>

Academic Editor: Jean-Michel Lafon

Received: 14 November 2022

Revised: 19 January 2023

Accepted: 20 January 2023

Published: 27 January 2023



Copyright: © 2023 by the authors. Licensee MDPI, Basel, Switzerland. This article is an open access article distributed under the terms and conditions of the Creative Commons Attribution (CC BY) license (<https://creativecommons.org/licenses/by/4.0/>).

1. Introduction

The Nanling metallogenic belt is the world’s most important W–Sn polymetallic province, with W–Sn deposits associated with S or A-type granites, such as the Dengfuxian, Yaogangxian, and Shizhuyuan deposits [1–4], as well as Cu polymetallic deposits associated with I-type granites, such as the Tongshanling deposit [5,6]. The grossular–grandite garnet, which forms in the generally oxidizing W–Sn skarn, is used to identify skarn types, interpret the skarn process, and constrain the metallogenic age [7,8]. Zhao et al. [9] compared the garnet properties of major and trace elements, revealing the skarn type, fluid evolution, and mineralization process of the Huangshaping W–Sn deposit (Figure 1). However, due to the deep invasion depth and high carbon content in the surrounding limestone, the W–Sn skarn associated with oxidized intrusion is generally reduced, characterized by massive pyroxene and less garnet [10,11]. The study of various W–Sn deposits reveals that W–Sn and Cu mineralization are primarily concentrated in the Cretaceous, Jurassic, and Triassic periods [12–14], with Cu polymetallic mineralization occurring approximately 5–10 Ma before W–Sn mineralization [11,14,15]. Nonetheless, the geochronology, trace element composition, and mineralization process of reductive skarn, which are rarely studied in the

Nanling metallogenic belt, prevent the correlation and metallogenic regularity of different skarn types in the Nanling metallogenic belt.

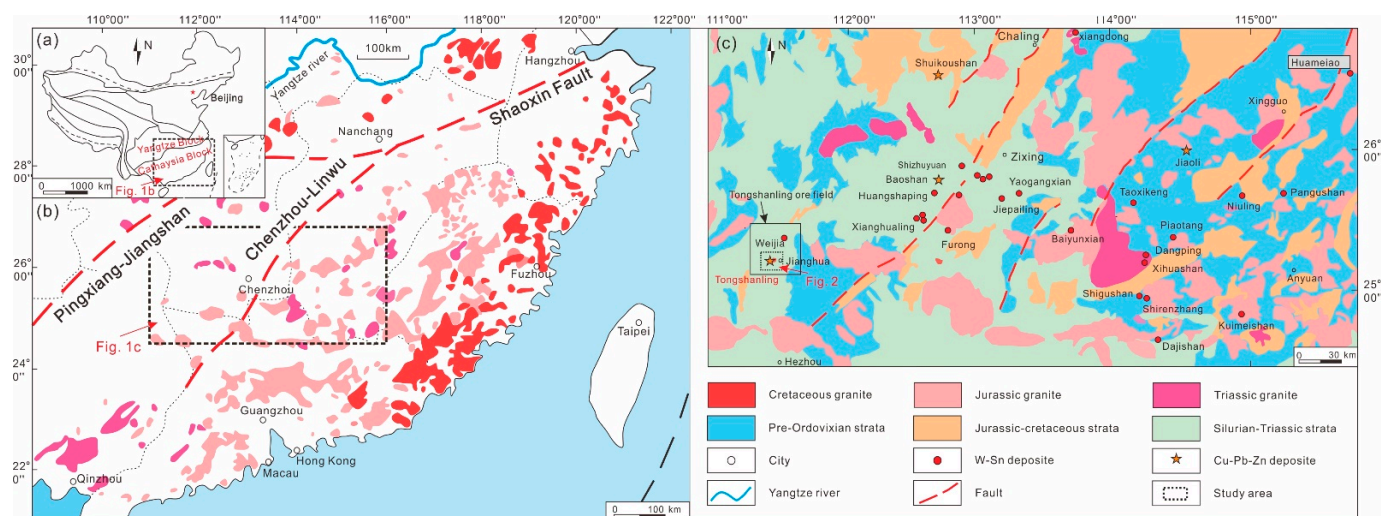


Figure 1. (a) Plate Tectonic Map of China. (b) Location of South Hunan district in the Qin-Hang Belt and the Nanling Region, modified from [16,17]. (c) Geologic map of Nanling metallogenic belt, modified from [11].

One of the most abundant minerals in the skarn deposit [10,18,19], garnet, is enriched in trace elements and fluid inclusions, with measured fluid evolution information such as temperature (T), pressure (P), pH, redox conditions (fO_2), and fluid components [10,20]. Grossular-andradite garnet ($Ca_3Al_2Si_3O_{12}-Ca_3Fe_2Si_3O_{12}$), associated with magmatic-hydrothermal fluids, is a preferred U–Pb dating mineral due to its high U and Th contents (several hundred ppb to several ppm [21–23]) and high U–Pb isotopic system closure temperatures (>850 °C) [24]. A mass of skarn deposits has been dated by this method [23,25,26]. The grossular-andradite garnet, which is usually used for dating research, mainly exists in oxidized skarn deposits, but it is also occasionally seen in reduced skarn deposits, such as the Darongxi W deposit in western Hunan [27], where the grossular-andradite garnet in reduced skarn deposits can also be used for dating research.

The Tongshanling deposit, located in the western part of the Nanling metallogenic belt, is a typically reduced skarn deposit associated with granodiorite [6,9,28], which primarily undergoes Cu–W–Pb–Zn mineralization. Although previous studies have demonstrated that the diagenetic age is 178–160 Ma [29–31], the mineralization age is 162–155 Ma [6,9,30], and the age range with a large span makes the precise determination of skarn age difficult. In addition, the Tongshanling deposit exhibits skarn alteration zone characteristics in space, with widely distributed garnets, effectively reflecting the evolution of ore-forming chronology and fluids.

This study focuses on garnet from different zonings and elevations of the Tongshanling deposit to reveal skarn age, major, and trace elements, combined with fluid-inclusion characteristics, fingerprinting the properties and evolution of ore-forming fluids in different spaces of the Tongshanling deposit and enriching the study of garnet zonation in reduced skarn. LA–ICP–MS U–Pb dating, electron probe microanalysis (EPMA), laser ablation inductively coupled plasma mass spectrometry (LA–ICP–MS), and microthermal analysis are used in the geochemical analyses.

2. Geological Setting

2.1. Regional Geology

During the Neoproterozoic (780–860 Ma), the South China plate was formed by the collision of the Yangtze and Cathaysia blocks (Figure 1a) [9,32–34]. The South China plate

has been subjected to multi-stage, large-scale magmatism, resulting in extensive partial melting of the crustal basement and the formation of widespread magmatic rocks. Magmatism occurred primarily in three stages: Triassic (about 251–205 Ma), middle Upper Jurassic (about 180–142 Ma), and Cretaceous (about 140–66 Ma) (Figure 1b) [16,17]. These occurrences resulted in the formation of numerous magmatic units, which were accompanied by economically significant hydrothermal W–Sn mineralization [11,17].

The magmatism of the three periods corresponds to three major metallogenic events in South China [17]. The Nanling Ore belt, located in the central region of South China (Figure 1b,c), with massive magmatic rock and W–Sn–Cu polymetallic mineralization [17,35], on account of the multi-stage tectonic activities of the Paleo-Tethys and Paleo-Pacific plates during the Middle Jurassic. The three periods of magmatism correspond to three major metallogenic events in South China [17]. The Nanling Range, located in central South China, has massive magmatic rocks and W–Sn–Cu polymetallic mineralization [17,35] because of the multi-stage tectonic activities of the Paleo-Tethys and Paleo-Pacific plates during the Middle Jurassic. The magmatite can be divided into two categories based on the types of granite and ore-forming elements: The W–Sn mineralization related to S or A-type granites, such as Shizhuyuan, Yaogangxian, and so on [2,36,37], and Cu polymetallic mineralization related to I-type granites, such as Tongshanling, Shuikoushan, and Baoshan Figure 1c, [9,38,39]. This region's metallogenic types are primarily skarn, quartz vein, and greisen [9,11].

The Tongshanling ore field is in the western metallogenic belt of Nanling (Figure 1c) [40], and the basement is primarily composed of Cambrian–Ordovician shallow sea clastic rocks, cherts, and carbonate rocks [9,26]. The region's primary deposits are the Tongshanling Cu–W polymetallic deposit and the Weijia W deposit [12]. The region's tectonic pattern is primarily controlled by three faults that strike roughly NE–SW, NW–SE, and E–W. Massive Mesozoic granites and granodiorites, such as Qitianling, Qianlishan, Xianglinpu, Jinjiling, and Xishan rocks, are found in the area. These intrusions are generally associated with skarn, greisen, and quartz-veined Cu–W–Sn mineralization [9,11,41].

2.2. Deposit Geology

The Tongshanling Cu–W polymetallic deposit is a medium-scale Cu–Pb–Zn polymetallic deposit located in the southwestern part of the Tongshanling ore field. The total ore reserves of Cu, Pb, and Zn reserves are 2.5×10^3 Mt [42], including metal reserves of 2.5 Mt Cu, 3.0 Mt Pb, 2.1 Mt Zn, and 175 t Ag [6,9]. The exposed sedimentary rocks of the ore district are composed of Devonian, Carboniferous, Permian, Jurassic, and Cenozoic strata (Figures 2 and 3). The orebodies are primarily found in Devonian and Carboniferous limestones, particularly thick limestones from the middle Devonian Qiziqiao formation and the lower Carboniferous Shidengzi formation. Massive folds and faults occur in the area, and the fold axis trend is primarily NNE-striking. The faults are primarily NNE and EW-striking, represented by F1 and F2, which are ore-controlling faults that cut through the mining area [9]. Furthermore, the granodiorite and quartz porphyry with silicification, dolomitization, and Cu–Pb–Zn mineralization developed near the fault zone (Figure 2). The No. I, II, and III intrusions are distributed from east to west, covering an area exceeding 12 km² (Figure 2). From the core to the rim of intrusion, the granodiorite changes from granodiorite porphyry to fine-grained granodiorite, this is most closely related to Cu–W mineralization. Hydrothermal alteration occurs primarily in the contact zone between granodiorite and surrounding rock, exposing the Cu–W–Pb–Zn mineralization and mineralization alteration zones, ranging from granodiorite to Middle Devonian limestone (Figure 3).

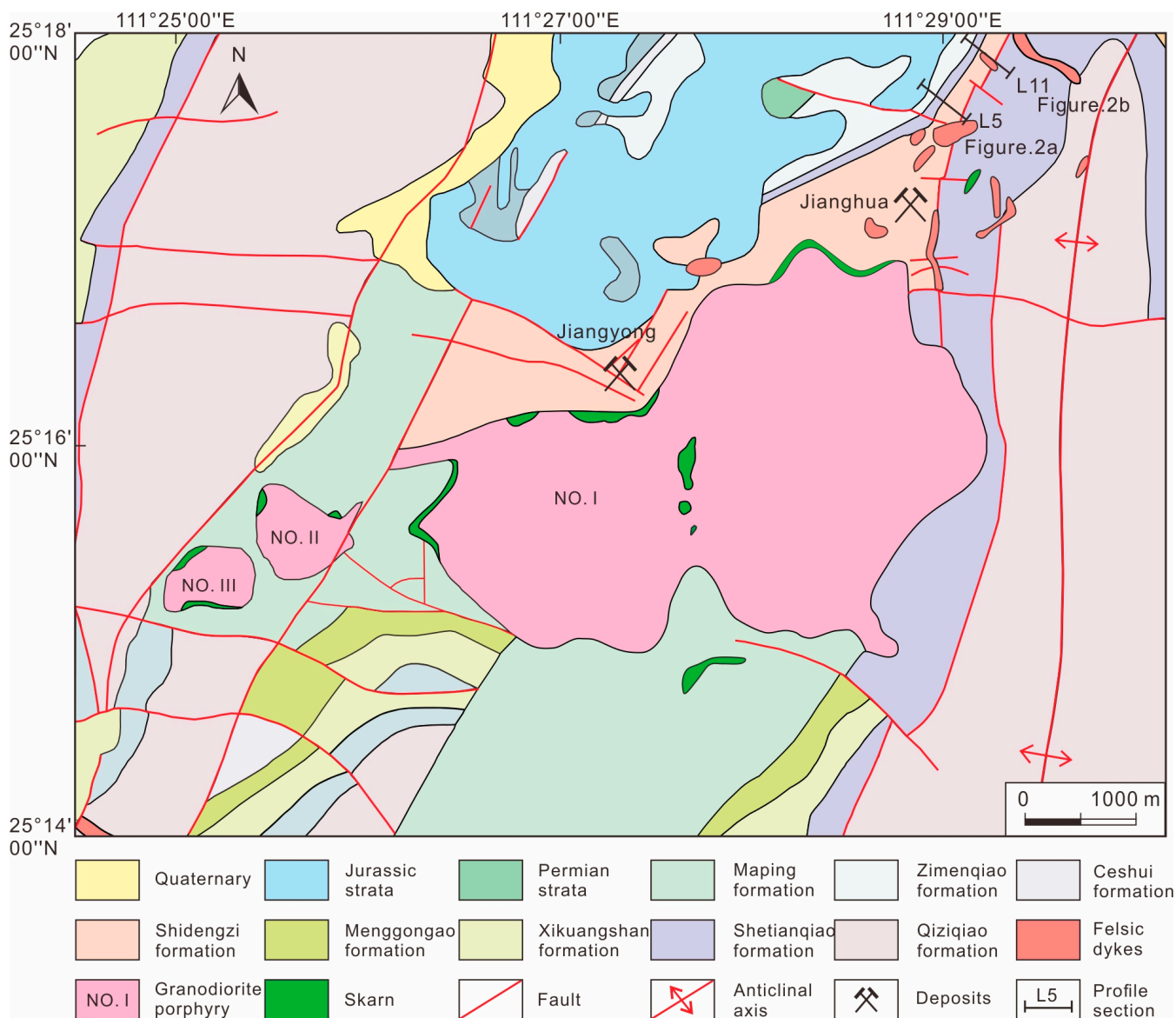


Figure 2. Geological map of the Tongshanling Cu polymetallic ore field, modified from [9].

Skarn zoning is visible from the center of the granodiorite to the limestone strata in the Tongshanling deposit (Figures 3 and 4j). The symbiotic sequence can be divided into three stages, from granodiorite to carbonate host rocks: prograde skarn, retrograde skarn, and quartz sulfide (Figure 5). The prograde skarn stage contains anhydrous silica minerals (e.g., diopside, wollastonite, and garnet) but no obvious mineralization (Figure 4a–c). The replacement of early silicate minerals (e.g., diopside and garnet) by late silicate minerals (e.g., epidote, chlorite, and actinolite) characterizes the retrograde skarn stage (Figure 4d–g). The main mineralization stage of Cu, W, Pb, and Zn is the sulfide stage, which consists of numerous quartz, sulfides, and minerals (such as pyrite, scheelite, pyrrhotite, sphalerite, and galena) (Figure 4h,i). The sulfide minerals superimpose on the prograde skarn, with discernible marble behind the sulfide belt (Figure 4h). A complete skarn alteration zone of this size is especially important for studying the metallogenic processes of the Tongshanling deposit.

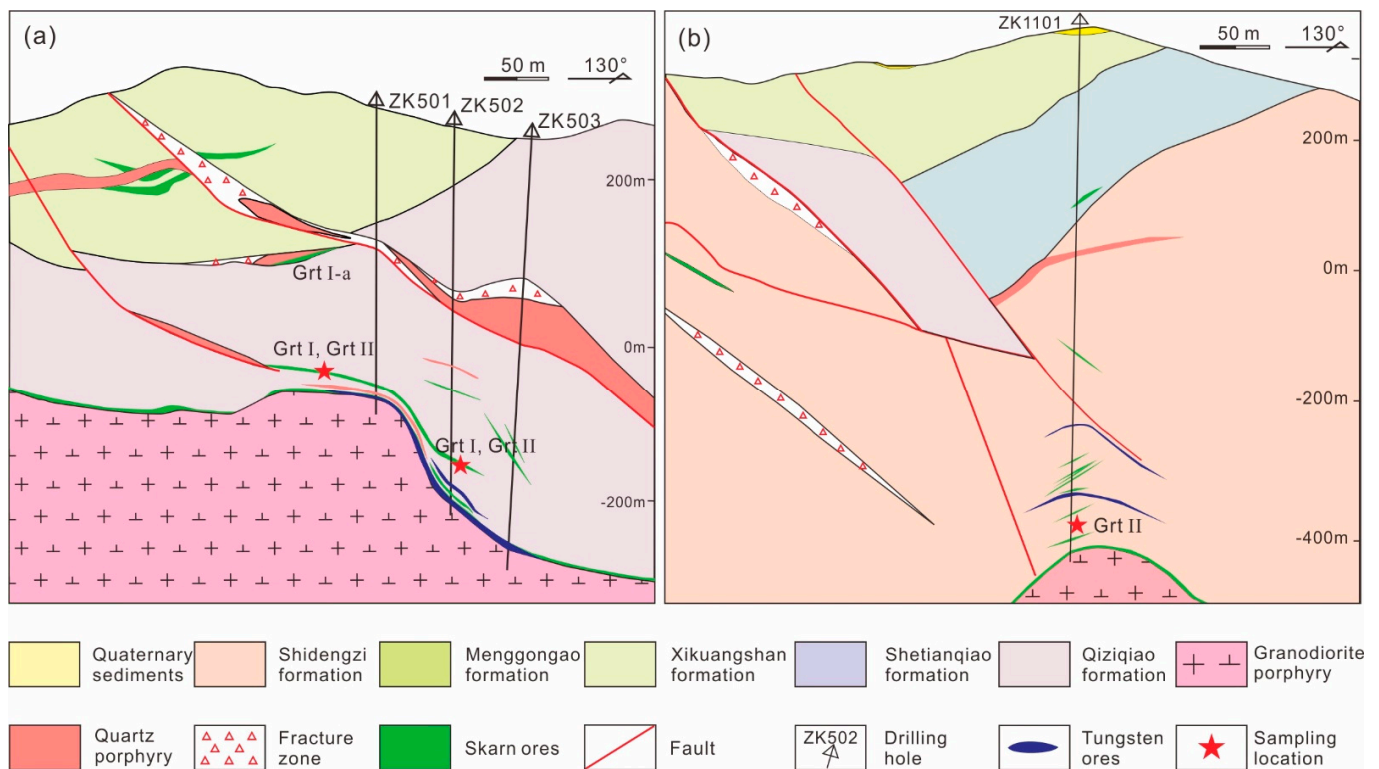


Figure 3. (a) No. 5 exploration line and sampling location of Tongshanling deposit; (b) No. 11 exploration line and sampling location of Tongshanling deposit.

Two kinds of garnets with distinct physicochemical properties are formed in the prograde and retrograde skarn stages of the Tongshanling deposit (Figure 4a–f). The garnets’ morphology; structure; and mineral assemblage differ noticeably. Garnet-I (Grt I) is a light green; brown; and orange massive aggregate formed in the prograde skarn stage near the granodiorite (Figure 4a–c). Grt I exhibit two characteristics: aggregates with no other mineral symbionts (Figure 4a); and symbiotic with diopside and wollastonite (Figure 4b,c). The garnet-II (Grt II) mineralization developed in the retrograde skarn stage; far away from granodiorite; is mainly veined and granular (Figure 4d–g); brown and orange (Figure 4d); symbiotic with quartz; chlorite; and epidote (Figure 4e–g); with late sulfide mineralization (pyrite; pyrrhotite; chalcopyrite; sphalerite; and galena) (Figure 4i).

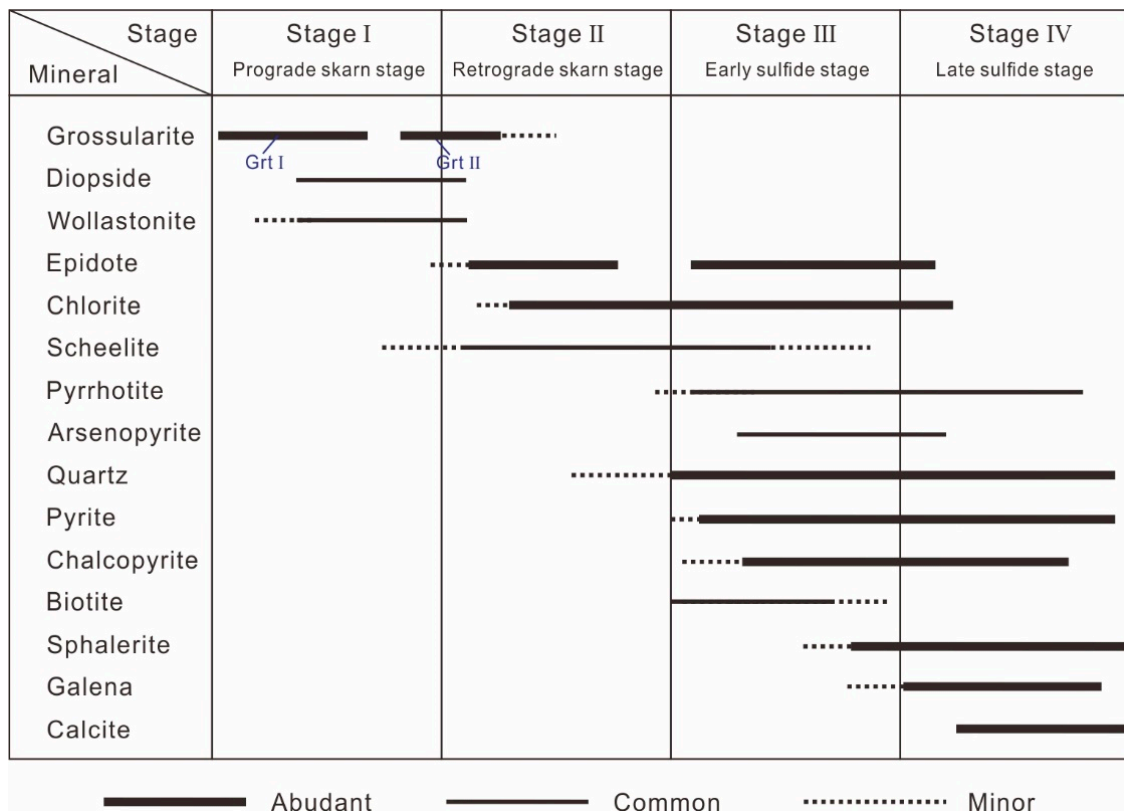


Figure 5. The paragenesis of minerals formed at various stages of the Tongshanling Cu–W–Pb–Zn polymetallic deposit.

3. Sampling and Methodology

3.1. Sample Descriptions

Six skarn garnet samples with varying depths (+90 m, +5 m, −35 m, −200 m, and −400 m relative to the sea level) are collected from the Tongshanling deposit's skarn contact zone and the sampling position is marked in Figures 3 and 4. The garnet samples are used for petrography analysis, U–Pb dating, and major and trace element analysis. The garnet samples were collected in the contact zone between granodiorite and limestone, with specific sampling information annotated in Figure 3. The geochemical analysis is performed on the collected samples after petrographic observation and SEM-back scattered electron (BSE) imaging. Petrographic observation and SEM–BSE imaging were performed at Central South University's Key Laboratory of Metallogenic Prediction of Nonferrous Metals and Geological Environment Monitor (Changsha, China). BSE imaging was conducted using a Sirion200 FE–SEM with a 30 kV accelerating voltage and a beam current of 15 nA. The following is the correlation analysis method:

3.2. EPMA

Major element analyses of the garnet samples were performed at the Key Laboratory of Metallogenic Prediction of Nonferrous Metals, Central South University (Changsha, China). The major elements were analyzed by using an electron probe micro-analyzer (EPMA-1720/1720H). The analytical conditions for spot analysis were as follows: an accelerating voltage of 15 kV, an electron beam current of 10 nA, and an electron beam diameter of 5 μm (spot size). The international SPI standards used were: $\text{NaAlSi}_3\text{O}_8$ for Al and Si, $\text{MgCaSi}_2\text{O}_6$ for Mg and Ca, TiO_2 for Ti, FeCr_2O_4 for Fe and Cr, and $\text{CaMnSi}_2\text{O}_6$ for Mn. The calibration method is absorption and fluorescence (ZAF), and the detection limits for most elements are 0.01 wt%. The precisions are <1% for element concentrations above 10 wt%,

<5% for element concentrations between 1 and 10 wt%, and >5% for element concentrations below 1 wt%.

3.3. Trace Element Analysis

LA-ICP-MS was used to analyze the trace elements in the garnet sample at the Wuhan Sample Solution Analytical Technology. (Wuhan, China). The detailed operating conditions for the laser ablation system and the ICP-MS instrument, as well as data reduction, are identical to those described by Zong et al. [43]. A GeolasPro laser ablation system with a COMPexPro 102 ArF excimer laser (wavelength of 193 nm and maximum energy of 200 mJ) and a MicroLas optical system was used for laser sampling. Ion-signal intensities were measured using an Agilent 7700e ICP-MS instrument. Helium was utilized as the carrier gas. Argon mixed with the carrier gas via a T-connector was used as the make-up gas. This laser ablation system includes a “wire” signal smoothing device [44]. In this study, the laser spot size and frequency were set to 40 μm and 9 Hz, respectively. The trace element compositions can be analyzed precisely in situ by LA-ICP-MS without applying internal standardization by applying an ablation yield correction factor on the basis of the normalization of the sum of all major element oxides to 100 wt% and using NIST 610 and USGS reference glasses BHVO-2G, BIR-1G, and BCR-2G as multiple reference materials for calibration [45]. Each analysis included a 20–30 s background acquisition followed by a 50 s data acquisition from the sample. Excel-based software, ICPMSDataCal, was used to perform offline signal selection and integration, time-drift correction, and quantitative calibration for trace element analysis [45]. The detection limits for most trace elements were 0.01 ppm.

3.4. In Situ U-Pb Dating

The in situ garnet LA-ICP-MS U-Pb dating was performed on an Analytikjena M90 quadrupole ICP-MS with a 193 nm NWR193 Ar-F excimer laser at the Yanduzhongshi Geological Analysis Laboratories Ltd. (Beijing, China). The downhole fractionation, instrument drift, and mass bias correction factors for Pb/U ratios of the grossular-andradite garnet were calculated using two analyses on the primary MALI Grandite (202 ± 2 Ma LA-ICP-MS; 202 ± 1.2 Ma ID-TIMS) [23], analyzed at the beginning of the session and in every ten unknown grossular-andradite garnets using the same spot size and conditions as the samples. The trace element contents of garnet were determined using SRM610 as an external standard and ^{29}Si as an internal standard element, assuming stoichiometric proportions. Each garnet analysis began with a 20-s blank gas measurement, followed by 40 s of analysis time when the laser was switched on. The garnet samples are collected on 45 μm spots with a laser at 9 Hz and a density of about $3\text{J}/\text{cm}^2$. A 0.6 L/min flow of the carrier gas carried particles ablated by the laser out of the chamber to be mixed with Ar gas and then transported to the plasma torch. The isotopes measured were ^{206}Pb , ^{207}Pb , ^{208}Pb , ^{232}Th , ^{235}U , and ^{238}U , with each element measured every 0.18 s and the Pb isotopes having a longer counting time than the other elements. The data reduction method was based on the detailed procedure described in [46], with an additional modification for correcting the trace amount of common Pb present in the standard using the ^{207}Pb correction of [47]. The detection limit for most elements was below 0.1 ppm, and the uncertainty is at level 1σ .

3.5. Fluid Inclusions

Microthermal analysis of fluid inclusions in quartz (closely associated with Grt II) was performed in the Key Laboratory of Metallogenic Prediction of Nonferrous Metals and Geological Environment Monitor at Central South University (Changsha, China) using LINKAMTHMSG 600 heating/freezing system (temperature range -196 to 600 $^{\circ}\text{C}$). When the temperature is below 0 $^{\circ}\text{C}$, the test accuracy of the micro-refrigerator is ± 0.1 $^{\circ}\text{C}$. The test accuracy is ± 0.1 $^{\circ}\text{C}$ in the 0 to 30 $^{\circ}\text{C}$ range, ± 1 $^{\circ}\text{C}$ in the 30 to 350 $^{\circ}\text{C}$ range, and ± 2 $^{\circ}\text{C}$ when the temperature exceeds 350 $^{\circ}\text{C}$. During the test, the heating rate near the phase transition point of aqueous inclusion was 0.2 $^{\circ}\text{C}/\text{min}$. The fluid salinity (W) was calculated

using the equation of freezing point temperature (T_m) and Bodnar [48] ($W = 1.78 T_m + 0.0442 T_m^2 + 0.000557 T_m^3$).

4. Results

4.1. Garnet Petrography

The Grt I and Grt II develop in different stages (Figure 5), and they reveal significantly different microstructure characteristics (Figure 6). Grt I particle sizes are 1.0–2.0 mm, with mostly euhedral or subhedral massive aggregates, light gray and colorless, and multiple visible fractures (Figure 6a–c). It is worth noting that Grt I has two distinct characteristics: early Grt I-a, a non-symbiotic mineral closer to the rock mass, and late Grt I-b, which is symbiotic with diopside and wollastonite (Figure 6a,b), with late pyrite filling occasionally observed in Grt I-b cracks (Figure 6c). The Grt II coexisting with quartz has preferred euhedral characteristics: sizes ranging from 0.5 to 5 mm, light gray and colorless, and visible fractures (Figure 6d–f). The rim of the Grt II is generally superimposed with retrograde skarn chlorite, epidote, other alterations, and mineralization.

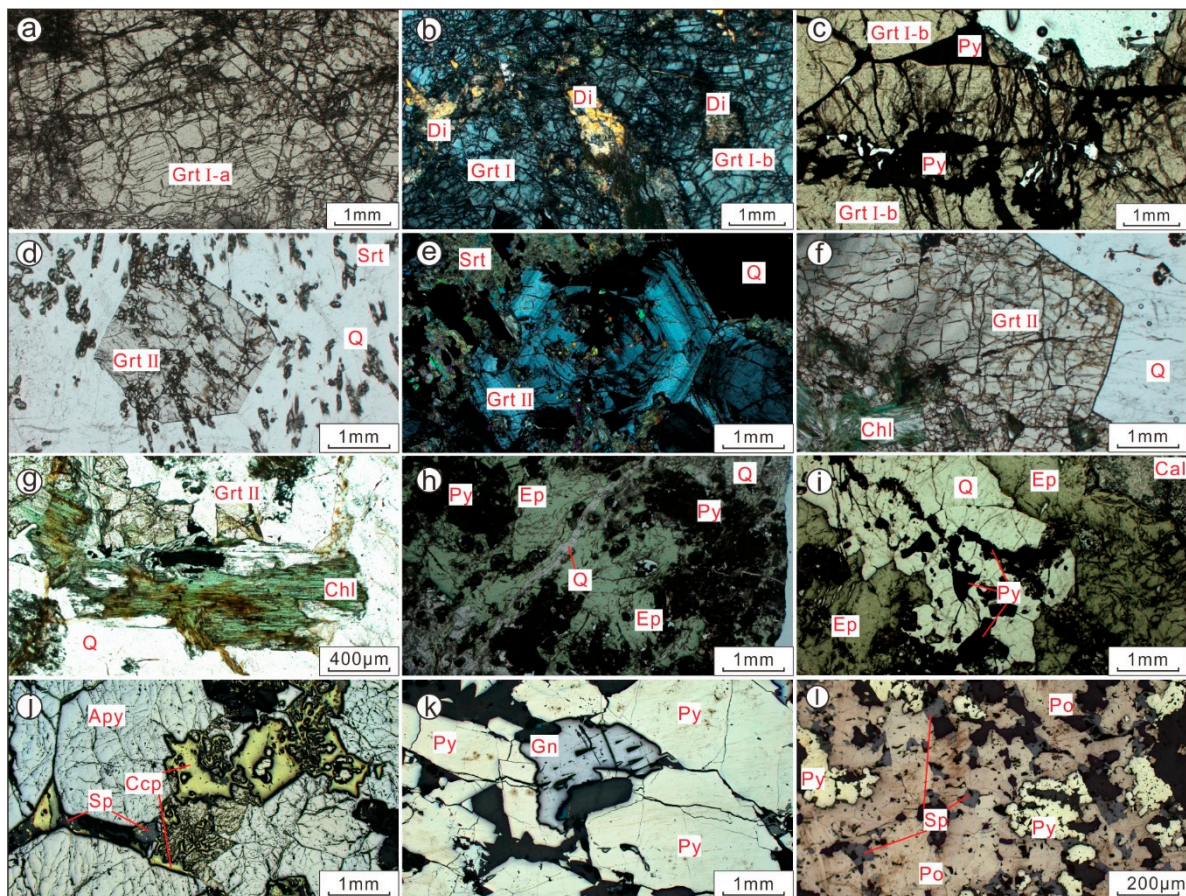


Figure 6. Micrographs show the petrographic characteristics and microstructure of skarn: (a) Graded skarn composed of Grt I, (b) primary skarn composed of Grt II with a small amount of diopside, (c) Grt II filled with a small amount of pyrite, no alteration, (d) Grt II associated with quartz, visible broken garnet particles; (e) Grt Is strongly altered by sericite, (f) garnet edge is replaced by chlorite, (g) the rim of Grt II is strongly replaced by chlorite, indicating pyrite mineralization, (h) epidote forms a symbiotic relationship with pyrite, and quartz veins are cut-off, (i) epidote is cut by quartz, and pyrite minerals are found in quartz veins, (j) symbiotic chalcopyrite and sphalerite grow along the arsenopyrite fissure, (k) coexistence of pyrite and galena, (l) pyrite, pyrrhotite, and galena symbiosis. Abbreviate: Grt = garnet, Di = diopside, Srt = sericite, Ep = epidote, Chl = chlorite, Q = quartz, Py = pyrite, Ga = sphalerite, Sp = galena, Po = pyrrhotite, Ccp = chalcopyrite, Apy = arsenopyrite.

The BSE image features of garnet formed at various stages differ. The Grt I lack an apparent zonation, as well as bright and dark areas. Furthermore, coarse pyrite particles and less quartz appear at the garnet rim, which differs from pyrite in the Grt I-b crack (Figure 7a–c), with the altered area still retaining the preferred garnet crystal boundary. The Grt II exhibited evident oscillatory zonation (Figure 7d), primarily at the garnet rim (Figure 7d–f), where the area of a single growth ring ranges from several microns to hundreds of microns. Grt II has distinct core and edge regions, with the core region typically consisting of an average or occasionally oscillating ring. The BSE images are dominated by bright bands, and the rim regions alternate between bright and dark bands. The rim also has an alteration zone of mineral cover in the retrograde skarn stage. The microscopic characteristics and BSE diagram distinguish three garnet areas: (a) the core area, (b) the rim area, and (c) the rim alteration area.

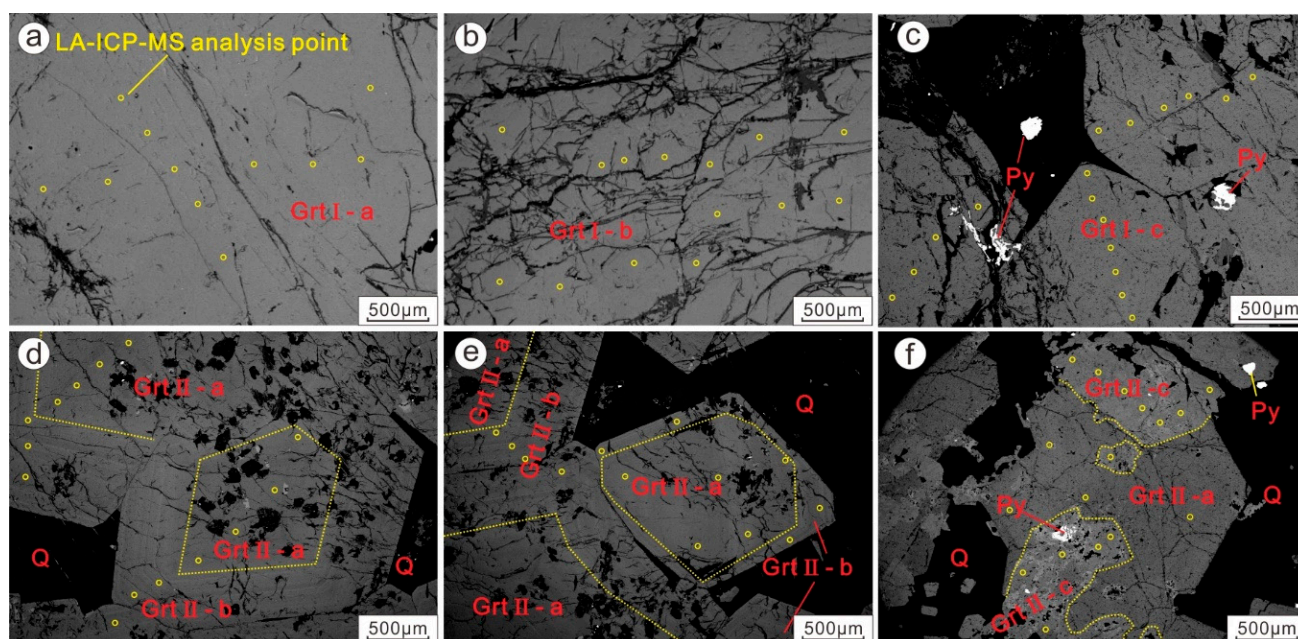


Figure 7. BSE images of the Grt I and Grt II at various stages of the Tongshanling Cu–W polymetallic deposit: (a) BSE image of massive Grt I-a with acyclic characteristics, (b) BSE image of Grt I-b, acyclic characteristics, (c) BSE image of Grt I-c, acyclic characteristics, pyrite can be seen in the cracks, (d) BSE image of Grt II-a core and Grt II-b edge, Grt II-b shows zonation features, (e) BSE images of Grt II-a core and Grt II-b margins, and (f) BSE images of Grt II-b and margin alteration region II-c showing pyrite superposition.

According to the microscopic and BSE image characteristics of garnet, selecting the typical samples for geochemical analysis. The analysis of main and trace elements in garnet are selected from Grt I and Grt II at different altitudes (+90 m, +5 m, −35 m, −200 m, and −400 m relative to the sea level), and the different divisions (a, b and c) of Grt I and Grt II are determined. The garnet grains chosen for U–Pb dating are the Grt I and Grt II of −15 m above sea level combined with the microscopic and display BSE image characteristics. The garnet grains without cracks, alteration, and oscillatory zonings are selected for U–Pb dating. Select samples of Grt II at different altitudes (+5 m, −35 m, and −400 m relative to the sea level) to test the temperature and salinity characteristics of fluid inclusions in quartz closely associated with Grt II.

4.2. Major Element Compositions

Based on microscopic and BSE image features, 77 LA–ICP–MS spots of Grt I and Grt II are analyzed with the LA–ICP–MS results presented in the (Supplementary Materials Table S1). The compositions of Grt I and Grt II are essentially the same, with the main

elements being Si, Ca, Al, and Fe, with a trace of Ti, Mn, and Mg (total content less than 5 wt%). The garnet particles in the Tongshanling deposit are dominated by the grossular–andradite (Figure 8), the Grt I component range ($\text{Gro}_{56.03}\text{And}_{39.00}$ – $\text{Gro}_{77.07}\text{And}_{15.85}$), the Grt II component range ($\text{Gro}_{70.63}\text{And}_{22.37}$ – $\text{Gro}_{77.74}\text{And}_{13.61}$); compared to the central BSE bright belt, Grt I exhibited higher aluminum content and lower iron content in the BSE dark and alteration belts. The Grt I from stage a to stage c, andradite content decreased (35–23 wt%), while grossular content increased (59–70 wt%). Grt II’s major element content is relatively consistent, with slight variation.

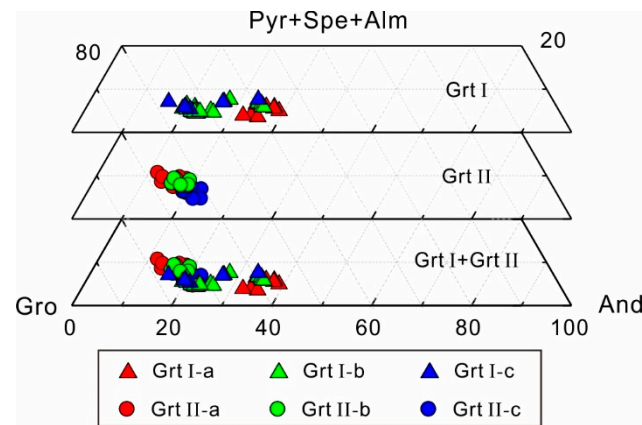


Figure 8. Classification diagram for Tongshanling garnet. Abbreviations: Gro = grossular; And = andradite; pyr = pyrope; spe = spessartine; Alm = almandine.

4.3. Trace Element Compositions

LA-ICP-MS trace element analysis results of garnet at various stages are shown in (Supplementary Materials Table S2). The Grt I has significantly lower large-ion lithophile element (LILE) concentrations (Cs: mean = 0.28, Rb: mean = 0.66 ppm, Ba: mean = 1.15 ppm, and Pb: mean = 0.03 ppm), whereas the Grt II concentration only decreased slightly (Cs: mean = 0.78 ppm, Rb: mean = 0.22 ppm, Ba: mean = 0.19 ppm, Pb: mean = 0.03 ppm). Furthermore, the Ti concentration of Grt I exceeds 1000 ppm (mean = 3198.79 ppm), whereas that of Grt II is much lower (mean = 381.62 ppm). Both garnets have U concentrations above the detection limit, with Grt I having a higher U concentration (Grt I: mean = 1.94 ppm and Grt II: mean = 0.38 ppm).

The REE characteristics of Grt I and Grt II differ noticeably (Figure 9): (1) Grt I has a higher ΣREE content (mean = 27.81 ppm) than Grt II (mean = 10.97 ppm); (2) Grt I and Grt II have different REE distribution patterns (Figure 9a–f), the Grt I is HREE enriched type with a negative Eu anomaly (Figure 9a,b), while the Grt II is HREE deficient type with a significant positive Eu anomaly with individual samples exhibiting significantly negative Ce anomaly (Figure 9d–f). (3). The total REE characteristics and distribution patterns of the garnet show consistent changes from the core to the rim (Figure 9a–f); the REE content of Grt I decreased significantly (81.58 ppm, 21.83 ppm, and 7.79 ppm, Figure 9a–c) with decreasing negative Eu anomaly, while the REE content of Grt II decreased similarly (29.53 ppm, 6.48 ppm, and 4.11 ppm as in Figure 9d–f) with Eu positive anomaly.

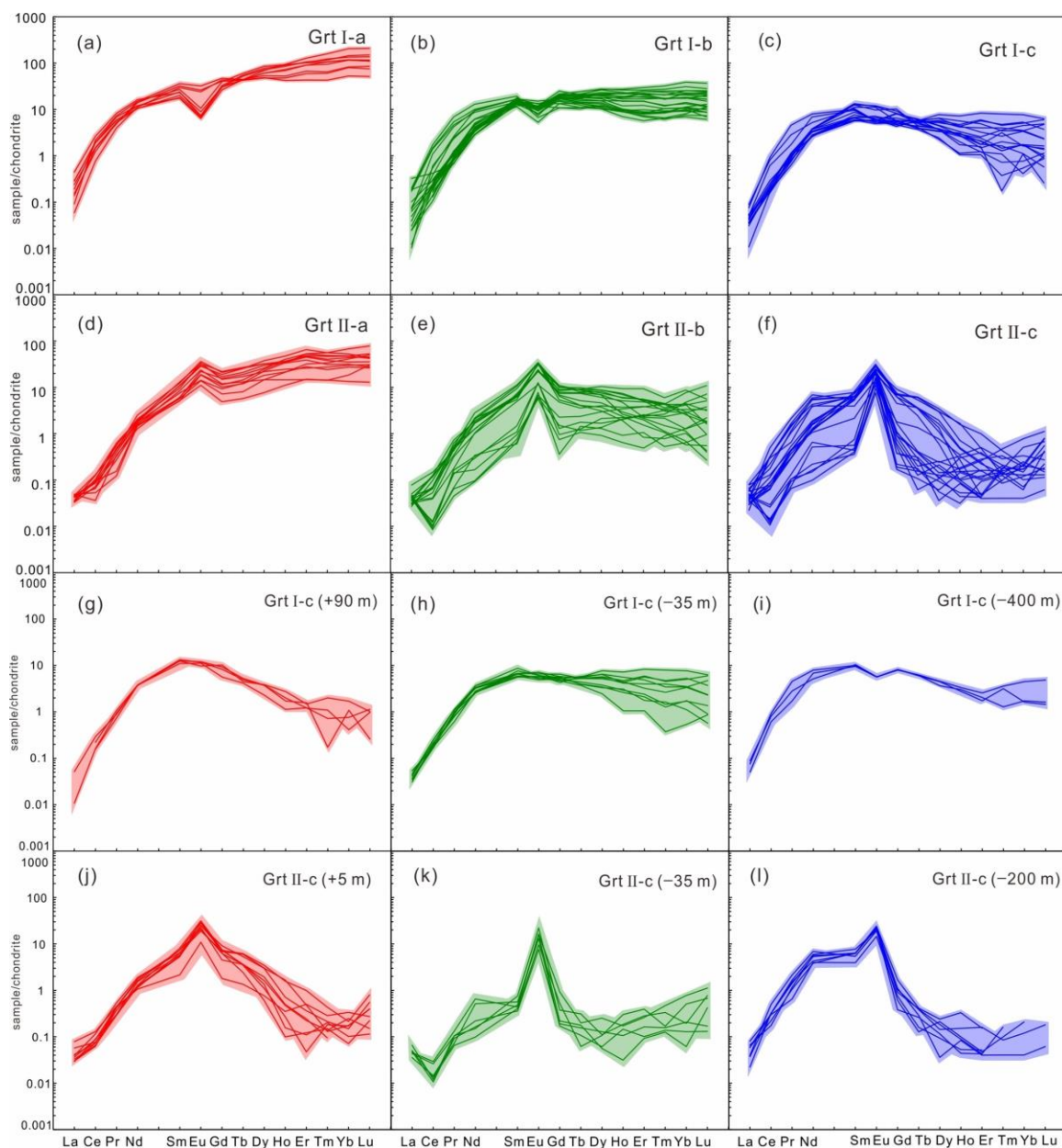


Figure 9. The standard REE patterns of Grt I and Grt II meteorites with varying elevations are divided into three sub-stages (a, b, c). The c-stage garnets (Grt I-c and Grt II-c) are selected for vertical comparison. (a) Grt I-a; (b) Grt I-b; (c) Grt I-c; (d) Grt II-a; (e) Grt II-b; (f) Grt II-c; (g) Grt I-c (+90 m); (h) Grt I-c (−35 m); (i) Grt I-c (−400 m); (j) Grt II-c (+5 m); (k) Grt II-c (−35 m); (l) Grt I-c (−200 m). The chondrite normalization values are from [49].

The REE elements of garnets at various depths show significant differences: (1) The Grt I-c at the different elevations exhibit similar REE patterns (Figure 9g–i) as well as the Grt II-c (Figure 9j–l); (2) The Σ REE content of Grt I is consistent from the shallow to deep-extracted samples (7.82 ppm, 7.17 ppm, and 9.83 ppm as in Figure 9g–i), with similar consistency observed in Grt II. However, the Σ REE content decreased due to LREE depletion at 35 m depth (5.51 ppm, 1.30 ppm, and 5.11 ppm, as in Figure 9j–l). (3) Garnets at various elevations exhibit a similar Eu anomaly (Figure 9g–l).

4.4. U-Pb Dating

The U–Pb isotopic data of Grt I and Grt II are shown in (Supplementary Materials Table S3). The Grt I samples were analyzed at 40 points, and the composition of 40 ablation points is 0.001–0.08 ppm Th, 0.02–0.96 ppm Pb, and 0.46–1.31 ppm U. The U/Pb ratio ranges from 0.93 to 39.00, with a mean of 15.14. Drawing 40 data points on the Tera–Wasserburg diagram yielded a lower intercept age of 165.4 ± 3.8 Ma (MSWD = 0.7) (Figure 10a), interpreted as the initiation age of skarn events. The Grt II samples analyze 40 points, where the compositions of 40 ablation points are: 0.75–57.90 ppm Th, 1.30–5.79 ppm common Pb, and 2.37–38.90 ppm U, with an average of 13.93 ppm. The U/Pb ratio ranges between 0.86 and 20.41, with an average of 5.05. A low intercept age of 159.5 ± 1.7 Ma (MSWD = 1.8) is obtained by drawing 40 data points on the Tera–Wasserburg diagram (Figure 10b), which is interpreted as the age of skarn mineralization.

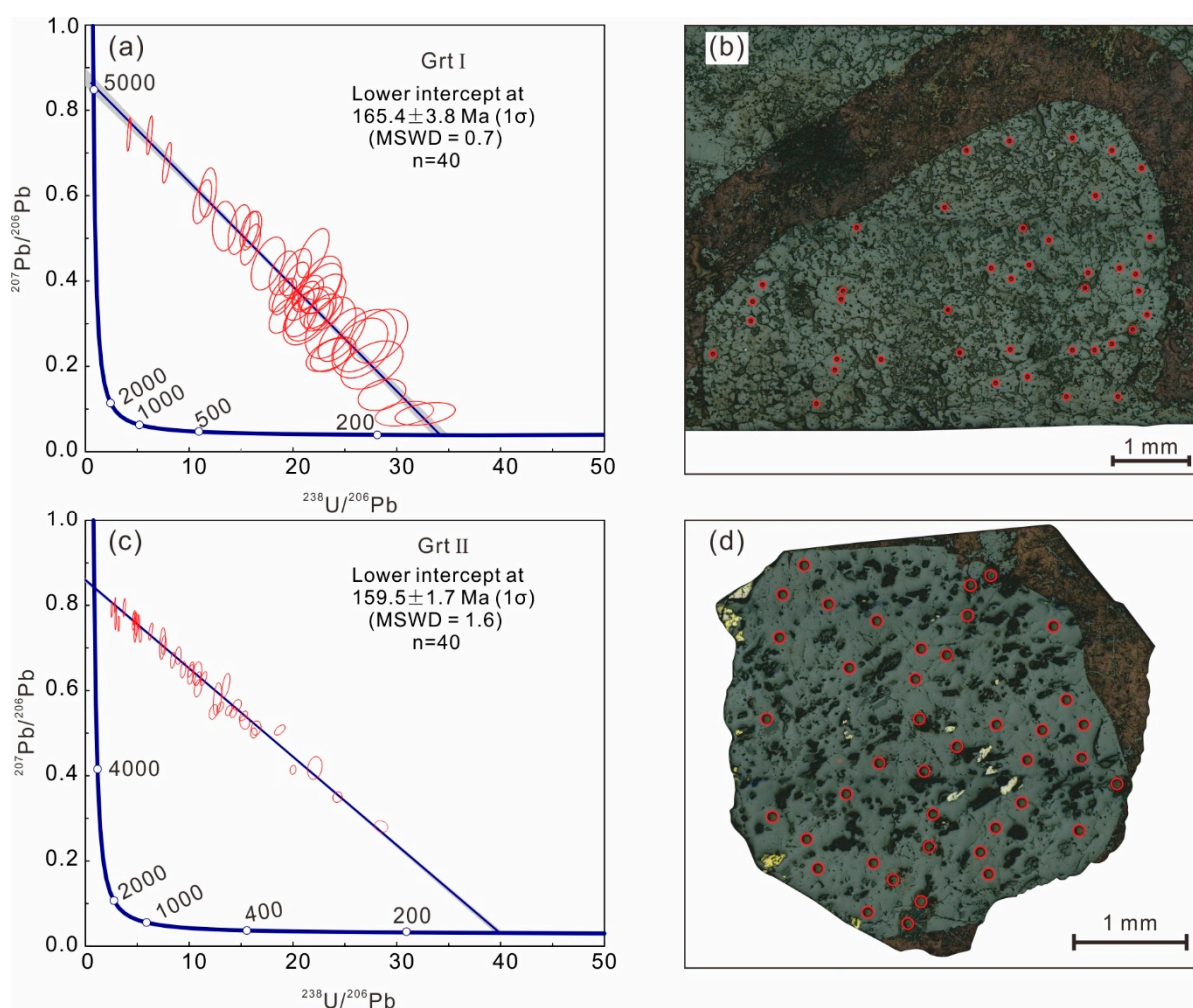


Figure 10. Results of U–Pb dating of garnet from the Tongshanling deposit: (a) U–Pb data synergy diagram of Grt I, (b) U–Pb dating analysis point of Grt I, (c) U–Pb data synergy diagram of Grt II, (d) U–Pb dating analysis point of Grt II.

4.5. Fluid-Inclusion Characteristics

Several fluids and isolated inclusions, primarily gas–liquid two-phase inclusions, can be seen in the quartz closely associated with Grt II (Figure 11). The liquid phase is the homogeneous state. The temperature and salinity test results of fluid inclusions are shown in (Supplementary Materials Table S4). The temperature measurements of quartz fluid inclusions at various depths (+5 m, −35 m, and −200 m) show that the temperature of +5 m fluid inclusions is 264–308 °C, with an average of 275 °C. Its salinity is 1.63–3.13 wt%

NaClea, with an average of 2.63 wt% NaClea. The homogenization temperature of −35 m fluid inclusions is 266–294 °C, with an average of 278 °C. Its salinity is 2.70–3.42 wt% NaClea, with an average of 3.16 wt% NaClea. The homogenization temperature of fluid inclusions, at an altitude of −200 m, is 270–335 °C, with an average of 301 °C and salinity of 2.26–3.71 wt% NaClea, with an average of 3.38 wt% NaClea.

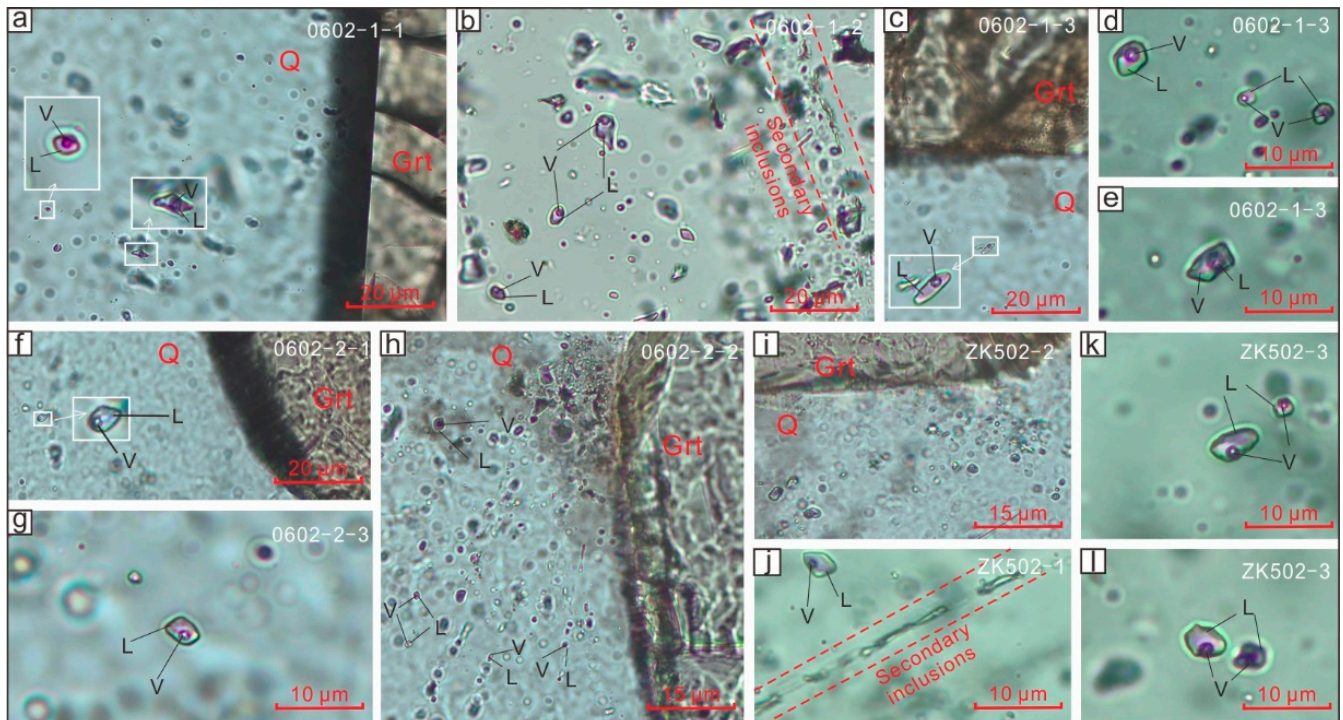


Figure 11. Microphotographs demonstrating the combination characteristics of fluid inclusions in quartz symbiotic with garnet at various depths (a–c,f–i,k) and characteristics of isolated fluid inclusions (d,e,j–l); a,b (+5 m); c–g (−200 m); h–l (−400 m). Abbreviations: L = liquid, V = vapor.

5. Discussion

5.1. Substitution Mechanism

The trace elements in garnet, particularly the REEs, can preferentially reflect the physical and chemical properties of the fluid during crystallization [50,51]. The garnet’s general formula is $X_3Y_2Z_3O_{12}$, where the X site represents divalent cations (e.g., octahedral coordinated Ca^{2+} , Mg^{2+} , Mn^{2+} , or Fe^{2+}), the Y site represents trivalent cations (e.g., octahedral coordinated Al^{3+} , Cr^{3+} , or Fe^{3+}), and the Z site is primarily tetrahedral-coordinated Si [51,52]. Trace elements primarily deposit in the garnet mineral lattice via four mechanisms: surface adsorption, occlusion, substitution, and interstitial solid solution [53]. REEs are deposited in the garnet by replacing divalent cations at the dodecahedral position, such as Ca^{2+} [51], as well as equivalent divalent cations substitution, such as Eu^{2+} . Furthermore, REE^{3+} substitution must be replaced by coupling substitution to maintain charge balance [51,54,55].

$$[X^{2+}]_{VIII} 2[X^+]_{VIII} + 1[REE^{3+}]_{VIII} + 1 \tag{1}$$

$$[X^{2+}]_{VIII} 1[REE^{3+}]_{VIII} + 1[Y^{3+}]_{VI} - 1[Y^{2+}]_{VI} + 1 \tag{2}$$

$$[X^{2+}]_{VIII} 1[REE^{3+}]_{VIII} + 1[Si^{4+}]_{IV} - 1[Z^{3+}]_{IV} + 1 \tag{3}$$

$$[X^{2+}]_{VIII} 3[]_{VIII} + 1[REE^{3+}]_{VIII} + 2 \tag{4}$$

where X^+ denotes Na^+ ; X^{2+} is mainly Ca^{2+} ; Z^{3+} denotes Al^{3+} or Fe^{3+} ; Y^{3+} is primarily substituted by Al^{3+} ; Y^{2+} denotes Mg^{2+} or Fe^{2+} ; $[]$ is a vacant Ca site, while VIII, VI, and IV represent coordination levels of 8, 6, and 4, respectively.

The garnet from Grt I and Grt II have significantly low Na content, which is insufficient to balance the cost of Ca^{2+} [55,56]. As a result, the substitution via Equation (1) can be ruled out. The negative Al vs. REE (Figure 12b) and positive Mg vs. REE (Figure 12c) correlations for Grt I indicate that REE^{3+} deposition in the garnet occurs via Equation (2) substitution, known as the menzerite substitution [54]. However, the correlations between REE and the elements Si, Al, Fe, and Mg in Grt II (Figure 12a–e) indicate that Equations (2) and (3) are not the main substitution mechanisms for REE^{3+} deposition. The negative Ca vs. REE (Figure 12f) indicates that REE^{3+} deposition into Grt II may have occurred through the Equation (4) mechanism via Ca site vacancy [57,58].

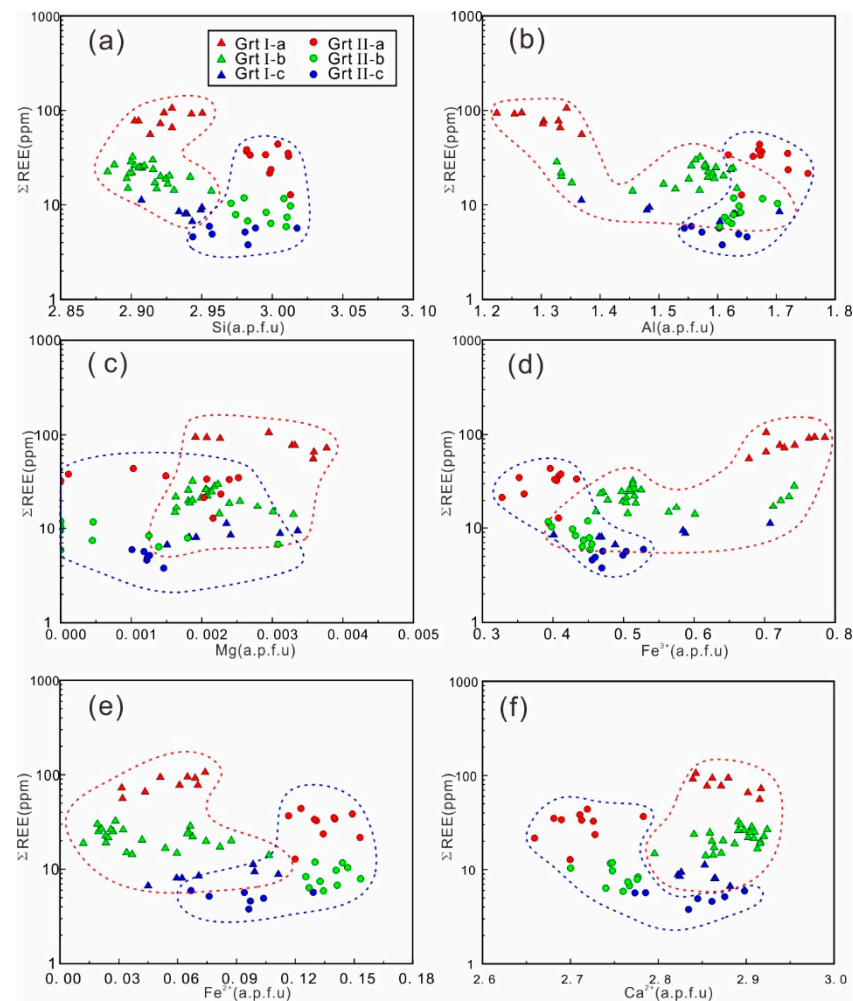


Figure 12. Binary plots of (a) Si (a.p.f.u) vs. ΣREE ; (b) Al (a.p.f.u) vs. ΣREE ; (c) Mg (a.p.f.u) vs. ΣREE ; (d) Fe^{3+} (a.p.f.u) vs. ΣREE ; (e) Fe^{2+} (a.p.f.u) vs. ΣREE ; (f) Ca^{2+} (a.p.f.u) vs. ΣREE .

The U element enters the garnet lattice primarily by substituting Ca^{2+} in the dodecahedral position [50], and the Grt I and Grt II (except Grt II-a) show a positive correlation between U and total REE, particularly LREE contents (Figure 13a–c), implying that U deposition into the garnet lattice is likely by coupling with LREE the dodecahedral position [8,19,50,59,60].

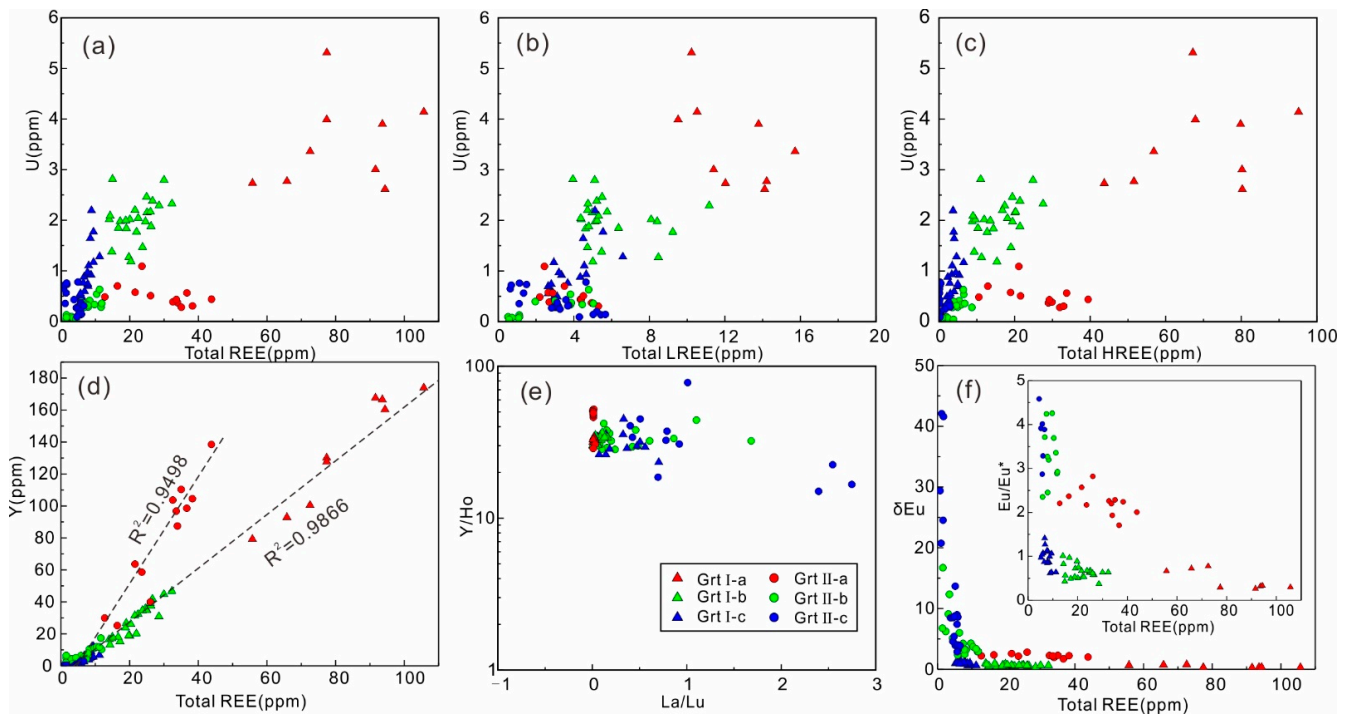


Figure 13. Binary plots of (a) Σ REE vs. U; (b) LREE vs. U; (c) HREE vs. U; (d) HREE vs. Y; (e) La/Lu vs. Y/Ho.; (f) Σ REE vs. δ Eu. The chondrite normalization values are from [49].

The geochemical data revealed that the geochemical behavior of element Y is very similar to that of REE^{3+} , with a significant correlation between Y and REE^{3+} (Figure 13d). The significant correlation between REE^{3+} and Y suggests that the deposition of REE^{3+} and Y into the garnet lattice is entirely controlled by crystal chemistry (e.g., coupling substitution mechanism) [55,61,62]. The stability of the Y and Ho ratio can indicate that the fluid and surrounding rock are in a state of equilibrium [55]. The Y/Ho values of Grt I and Grt II are relatively concentrated (Figure 13e, in an order of magnitude), showing that the skarn fluid is in a relatively balanced state during crystallization, the Y_o/Ho ratio range and Grt II-c fluctuates greatly (Figure 13e), which is reflected in the Grt II-c stages, the equilibrium state of skarn fluid is weakened.

5.2. Formation Age of Skarn

Granodiorite is the main intrusion related to mineralization in the Tongshanling deposit. Its diagenesis and mineralization age have been extensively studied [6,9,63]. Previous researchers dated a long formation span ranging from 178.9 Ma to 148.3 Ma with a peak of 165–160 Ma [6,30,63–65]. The wide age ranges of zircon U–Pb dating that No. I granodiorite in the east and No. III granodiorite (Figure 1b) in the west are 166.6 ± 0.40 Ma and 148.3 ± 0.35 Ma, respectively [65]. Many methods were used to restrain the mineralization age, such as garnet Sm–Nd and molybdenite Re–Os, with a mineralization age range of 173 to 155 Ma with a peak range of 160 to 155 Ma [9,30,40]. The age of mineralization in the Tongshanling area is coupled with the crystallization age of intrusives in time. In addition, the crystallization age of intrusives of other Cu polymetallic deposits (Baoshan and Shuikoushan deposit, Figure 1c) in the Nanling ore belt is 161–158.8 Ma, and the age of mineralization is 160–157.8 Ma [66,67].

The grossular–andradite with a high U content and a low Pb content is a preferred U–Pb dating tool [19,68,69], and the garnets from the Tongshanling deposit meet this requirement (Grt-I ^{238}U , ^{206}Pb , ^{207}Pb , 0.94 ppm, 0.03 ppm, 0.02 ppm, Grt-II ^{238}U , ^{206}Pb , ^{207}Pb , 12.35 ppm, 0.81 ppm, 0.49 ppm). Meanwhile, there are no obvious U-bearing mineral inclusions in the garnet, providing new evidence for the validity of the garnet LA–ICP–MS U–Pb age. Geochemical data show a positive relationship between U and total REE,

LREE, and HREE (Figure 13a–c), implying that U deposition in the garnet is primarily influenced by equilibrium crystal chemistry and surface adsorption [50,70]. The poor correlation between U and HREE in Grt II suggests that U entering Grt II is influenced by other conditions (Figure 13a–c) [50,70]. Hence, the U content in the garnet studied is primarily from the lattice, demonstrating the accuracy and applicability of garnet U–Pb dating. At the same time, the zircon U–Pb age of granodiorite (near the Grt I-a, Figure 4a) is 167.6 ± 0.6 Ma [6], and the cassiterite U–Pb age is 162.6 ± 2.0 Ma, which is consistent with the U–Pb age of Grt II. Overall, the age of skarn in the Tongshanling deposit is 165.4–159.5 Ma, which is consistent with the diagenetic and metallogenic age of the Tongshanling deposit obtained by predecessors [6,9,30,40], reflecting that the thermal metamorphism and hydrothermal metasomatism time of Tongshanling deposit are the middle Upper Jurassic, and the time of thermal metamorphism is slightly earlier.

5.3. Evolution of Hydrothermal Fluids

5.3.1. Temperature and Composition

Heterogeneity FIA (fluid inclusion assemblage) has a good petrological definition of hydrothermal garnet [71]. The fluid inclusions in the FIAs with a low gas/liquid ratio have similar homogenization temperatures (Figure 10), indicating fluid boiling during garnet formation. As a result, the temperature and pressure conditions of captured fluid inclusions can be directly limited by these heterogeneously captured FIAs [72]. The formation temperature of heterogeneous FIA is represented by its minimum homogenization temperature [73,74]. Previous research has shown that the homogenization temperature of quartz fluid inclusions does not decrease significantly from the retrograde to the quartz-sulfide stage [75]. Furthermore, there is no discernible change in the temperature characteristics of the Tongshanling deposit in the horizontal direction. Late garnet and quartz fluid inclusions associated with garnet reveal a fluid temperature of 264–335 °C (mean = 285 °C) during garnet crystallization. The temperature characteristics at different depths differ (+5 m: 275 °C on average; –35 m: 278 °C on average; –400 m: 301 °C on average), indicating that the temperature rises noticeably with depth (Figure 14a), and the fluid inclusions show fluid salinity changes of 1.63–3.71 wt% (+5 m: 2.66 wt% on average; –35 m: 3.17 wt% on average; –400 m: 3.44 wt% on average), indicating that the salinity rises noticeably with depth (Figure 14a). The difference in temperature and salinity at different depths of the Tongshanling deposit may be related to atmospheric precipitation and wall rock [6,11].

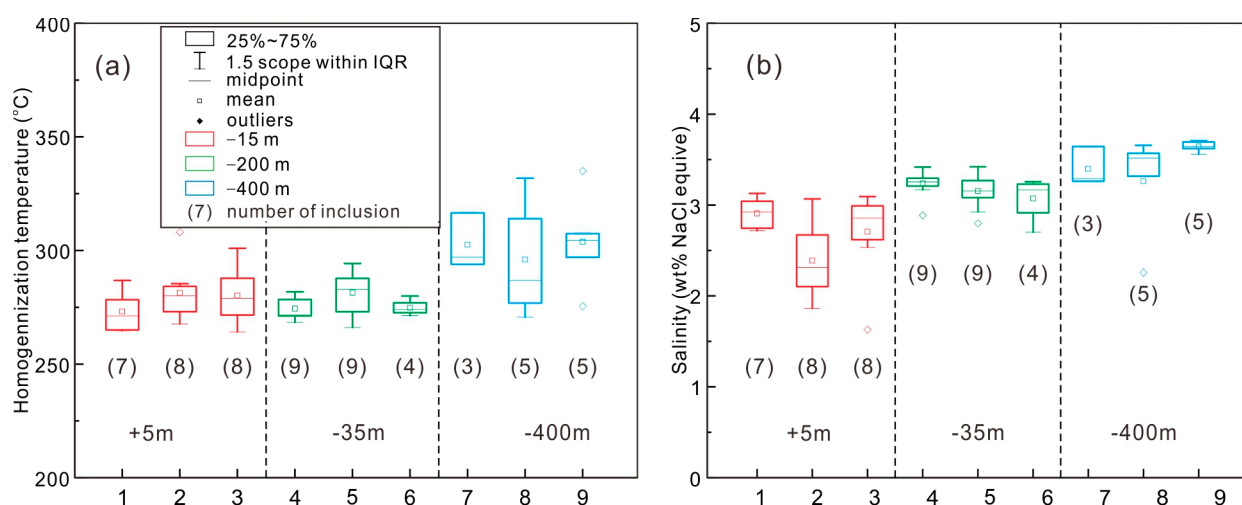


Figure 14. Analysis results of quartz fluid inclusions. (a) Temperature maps of quartz fluid inclusions at various depths; (b) Salinity maps of quartz fluid inclusions at various depths.

5.3.2. Oxygen Fugacity (fO_2)

The U, a redox-sensitive element, is significantly affected by fO_2 [50] and can be used to estimate fO_2 during garnet formation. Generally, U^{4+} is more compatible with garnet than U^{6+} because of its similar ionic radius with Ca^{2+} [49,50,76–78]. When fO_2 rises, U^{4+} tends to transform into U^{6+} , resulting in a decrease in U content in garnet, making U content a good indicator of fO_2 in skarn mineralization fluids. As a result, variations in U concentrations in different sections of garnet and in different garnet crystals can indicate the relative fO_2 of hydrothermal fluids during garnet crystallization [62].

The U can be found in both types of garnet species at the Tongshanling deposit. The early Grt I has higher U content (0.49–5.31 ppm, average 1.98 ppm) than the late Grt II (0.02–1.09 ppm, average 0.38 ppm) (Figure 13a), indicating that the Grt I crystallized under relatively low fO_2 , namely, the fO_2 from granodiorite intrusion to carbonate rock gradually increases during garnet crystallization. Besides, from stage a to stage c, the U contents of the Grt I decrease while the Grt II have no change (Figure 13a), this implies that the fO_2 of Grt I increases during crystallization, while the Grt II is relatively stable. Nonetheless, the U element content of the Grt I-c and Grt II-c at different elevations varies slightly, indicating that the garnets have similar fO_2 .

5.3.3. pH

Studies have shown that one of the factors controlling water–rock interaction is the REEs fractionation in skarn hydrothermal solutions, affected by environmental pH [26,76–78]. The Eu element in fluids has two valence states of Eu^{2+} and Eu^{3+} , the Eu^{3+} in the fluid does not cause the fluid to show Eu anomaly, while the extra Eu^{2+} will make the fluids show positive Eu anomaly characteristics. Under nearly-neutral pH conditions, the chondritenormalized REE patterns of the skarn fluids are HREE-enriched and LREE-depleted with negative or no Eu anomalies. Refs. [26,77,78], whereas, fluids in weak acidic conditions, the REE patterns are more controlled by the presence of Cl^- in the fluids. Under weak acidic pH conditions, it can enhance the stability of soluble Eu^{2+} ($EuCl_4^{2-}$ is the dominant species) and lead to obvious positive Eu anomaly [8,31].

Early Grt I-a has significantly enriched HREEs, whereas LREEs are relatively depleted, with obvious negative Eu anomaly characteristics (Figure 9a), indicating that the environmental conditions in the prograde skarn may be close to neutral pH [76]. The LREEs contents of Grt I-b and Grt I-c are constant, whereas the HREE contents decrease, and the negative Eu anomaly weakens (Figures 9b,c and 13f), indicating that there is no discernible change in pH. The HREEs content decreases, as does the negative Eu anomaly, ascribed to the nature of early intrusions [79]. The REEs fractionation of Grt II-a exhibits a clear positive Eu anomaly (Figure 9d), indicating that it is formed at a pH close to acidity. In Grt II-b and Grt II-c stages, the Eu anomaly is more obvious (Figures 9e,f and 13f), indicating that the Eu^{2+} content in the fluid increases, the reaction fluid tends to an acidic environment, and pH decreases. Hence, from the prograde skarn stage (Grt I) to the retrograde skarn stage (Grt II), the pH of skarn fluid is decreasing. The increase of Cl^- concentration also indicates higher salinity characteristics in the Grt II stage. However, The Grt I and Grt II at different elevations show the same REE pattern with the same Eu anomaly (Figure 9g–i), indicating that the elevation had no indigenous effect on REE deposition into the garnet lattice.

5.4. Spatio-Temporal Zoning of Skarn

The geochemical properties of Grt I indicate that its growth is primarily controlled by crystal chemistry in the prograde skarn stage [55,61,62], indicating that the contact zone between granodiorite and carbonate rocks primarily experiences thermal metasomatism and is in a relatively closed environment [51], whereas Grt I has no oscillating region and only irregular crystals (Figures 6a–c and 7a–c). The Grt II-a and Grt I have similar REE patterns (except Eu, which may be caused by pH change), indicating that Grt II and Grt I have the same fluid source [6]. The difference in rare earth patterns may be caused by changes in the physical and chemical environment. The Grt II-b formed in the retrograde

skarn stage has distinct oscillatory zonation (Figures 6d–f and 7d–f), indicating that the fluid was in an open system at the time, and the composition fluctuated continuously, accompanied by multiple metasomatic pulses [10,51]. The garnet exhibits obvious oscillatory zonation characteristics for some Grt II-b (Figures 6e and 7d), ascribed to a coupled dissolution–reprecipitation mechanism [80,81].

The fluid evolution in the horizontal direction of the Tongshanling deposit mainly depends on time and physicochemical conditions (Figure 15a,b). The chronological results of Grt I and Grt II indicate that the skarn event in the Tongshanling deposit mainly occurred in the middle Upper Jurassic, and the crystallization time of Grt I is earlier than that of Grt II. The trace element characteristics (especially REEs) of Grt I and Grt II show that the characteristics of skarn fluid have changed from the prograde skarn stage to the retrograde skarn stage, mainly showing the decrease of pH, fO_2 and total REE (especially HREE), which may be related to the multiple activities of Tongshanling granodiorite and mineral crystallization, and the increase of salinity may be related to the surrounding rock.

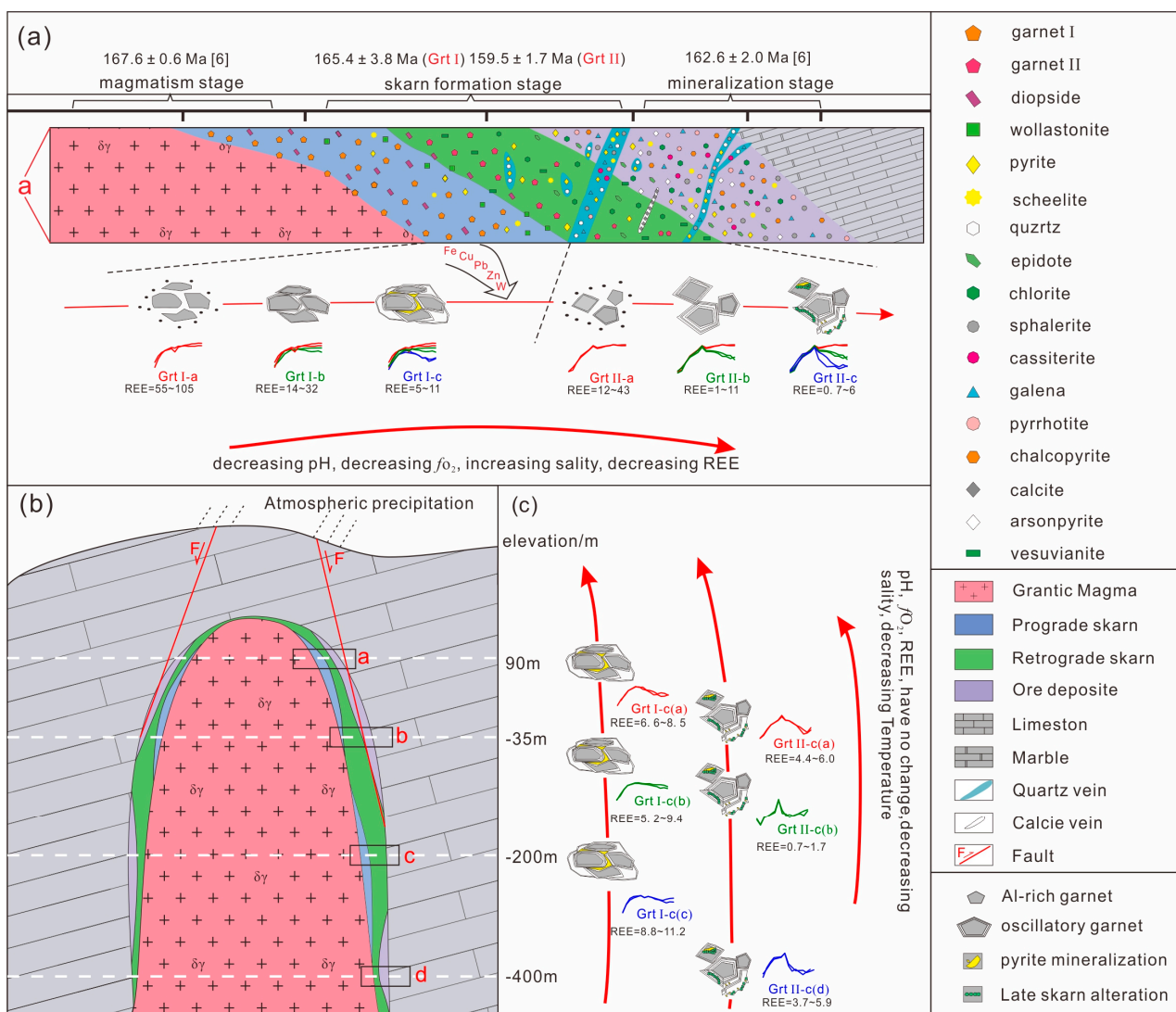


Figure 15. Spatial-temporal distribution evolution model of different types of garnets in the Tongshanling deposit. (a) Schematic diagram showing the horizontal textural and formation condition evolution of the Tongshanling garnet; (b) Schematic diagram showing horizontal and vertical zoning of skarn in Tongshanling deposit; (c) Schematic diagram showing the horizontal textural and formation condition evolution of the Tongshanling garnet.

The garnets at different elevations show no obvious zonation characteristics (Figure 15c), while the salinity in the shallow part is clearly reduced due to the addition of shallow atmospheric water [11], indicating that pressure has little effect on the REE pattern of garnet. Hence, the geochemical composition of garnet can reflect changes in the physical and chemical environment of the garnet crystallization fluid of garnet, and clearly reflect the spatio-temporal variation characteristics of the deposit, which provides a significant reference for studying the evolution of the mineralization process.

6. Conclusions

- (1) The age of garnet crystallization in the prograde skarn stage is about 165.4 Ma, and the crystallization age of garnet in the retrograde skarn stage is about 159.5 Ma, indicating that the thermal metamorphism and hydrothermal metasomatism of the Tongshanling deposit occurred in the middle Upper Jurassic, and the thermal metamorphism is slightly earlier.
- (2) The geochemical characteristics of Grt I and Grt II indicate that the physicochemical environment of skarn fluid has changed from the progradational skarn stage to the retrograde skarn stage, which is mainly manifested in the decrease of pH, fO_2 , and REE content and the increase of salinity.
- (3) The garnet has high salinity, temperature, and pressure in the deep region along the vertical direction, while the pH, fO_2 , REE content, and REE pattern have no change.
- (4) Garnet U–Pb dating provides a good constraint on the duration of progressive and retrograde metamorphisms. In addition, because trace elements are sensitive to their physical and chemical environments, they can be used to investigate spatio-temporal zoning.

Supplementary Materials: The following are available online at <https://www.mdpi.com/article/10.3390/min13020187/s1>, Table S1: Major element compositions (wt%) of garnet in the Tongshanling Cu–W polymetallic deposit, Table S2: Distribution characteristics of trace elements in garnet I and garnet II from the Tongshanling Cu–W polymetallic deposit, Table S3: LA-ICP-MS U–Pb isotope of garnet from the Tongshanling Cu–W polymetallic deposit, Table S4: Characteristics of liquid-rich fluid inclusions of Quartz(Symbiosis with garnet II) in Tongshanling Cu–W polymetallic deposit.

Author Contributions: Conceptualization, F.T., H.K. and B.L.; Data curation, F.T. and B.L.; Formal analysis, F.T. and Q.W.; Funding acquisition, H.K. and Q.W.; Investigation, F.T. and B.L.; Methodology, F.T. and H.K.; Project administration, H.K.; Resources, B.L. and F.T.; Supervision, H.K.; Validation, F.T. and B.L.; Visualization, F.T.; Writing—original draft, F.T. and B.L.; Writing—review and editing, F.T. and S.C. All authors have read and agreed to the published version of the manuscript.

Funding: This work was financially supported by the National Key Research and Development Plan (Grant No. 2018YFC0603901 and No. 2018YFC0603902) and the Postgraduate Research and Innovation Project of Central South University (independent exploration) (2022ZZTS0458).

Data Availability Statement: Data are contained within the supplementary materials.

Acknowledgments: We appreciate editors and reviewers for their thoughtful and constructive reviews on the manuscript.

Conflicts of Interest: The authors declare no conflict of interest.

References

1. Chen, J.; Wang, R.; Zhu, J.; Lu, J.; Ma, D. Multiple-aged granitoids and related tungsten-tin mineralization in the Nanling Range, South China. *Sci. China Earth Sci.* **2013**, *56*, 2045–2055. [[CrossRef](#)]
2. Chen, Y.X.; Li, H.; Sun, W.D.; Trevor, I.; Tian, X.F.; Hu, Y.B.; Yang, W.B.; Chen, C.; Xu, D.R. Generation of Late Mesozoic Qianlishan A2-type granite in Nanling Range, South China: Implications for Shizhuyuan W–Sn mineralization and tectonic evolution. *Ore Geol. Rev.* **2016**, *266–267*, 435–452.
3. Wang, X.; Ren, M.H. Constraints of hydrothermal and magmatic zircon on the origin of the Yaogangxian tungsten deposit, southern China. *Ore Geol. Rev.* **2018**, *101*, 453–467. [[CrossRef](#)]

4. Cao, J.Y.; Wu, Q.H.; Yang, X.Y.; Deng, X.T.; Li, H.; Kong, H.; Xi, X.S. Geochemical factors revealing the differences between the Xitian and Dengfuxian composite plutons, middle Qin-Hang Belt: Implications to the W-Sn mineralization. *Ore Geol. Rev.* **2020**, *118*, 103–353. [[CrossRef](#)]
5. Li, X.F.; Hu, R.Z.; Hua, R.M.; Ma, D.S.; Wu, L.Y.; Qi, Y.Q.; Peng, J.T. The Mesozoic syntexis type granite-related Cu-Pb-Zn mineralization in South China. *Acta Petrol. Sin.* **2013**, *29*, 4037–4050. (In Chinese)
6. Wu, J.H.; Kong, H.; Li, H.; Thomas, J.; Algeo, C.D.E.; Kotaro, Y.; Liu, B.; Wu, Q.H.; Zhu, D.P.; Jiang, H. Multiple metal sources of coupled Cu-Sn deposits: Insights from the Tongshanling polymetallic deposit in the Nanling Range, South China. *Ore Geol. Rev.* **2021**, *139*, 104521. [[CrossRef](#)]
7. Yang, Y.L.; Ni, P.; Wang, Q.; Wang, J.Y.; Zhang, X.L. In situ LA-ICP-MS study of garnets in the Makeng Fe skarn deposit, eastern China: Fluctuating fluid flow, ore-forming conditions and implication for mineral exploration. *Ore Geol. Rev.* **2020**, *126*, 103725. [[CrossRef](#)]
8. Zhao, L.J.; Zhang, Y.; Shao, Y.J.; Li, H.B.; Sajjad, A.S.; Zhou, W.J. Using garnet geochemistry discriminating different skarn mineralization systems: Perspective from Huangshaping W-Mo-Sn-Cu polymetallic deposit, South China. *Ore Geol. Rev.* **2021**, *138*, 104–412. [[CrossRef](#)]
9. Zhao, P.L.; Yuan, S.D.; Mao, J.W.; Santosh, M.; Li, C.; Hou, K.J. Geochronological and petrogeochemical constraints on the skarn deposits in Tongshanling ore district, southern Hunan Province: Implications for Jurassic Cu and W metallogenic events in South China. *Ore Geol. Rev.* **2016**, *78*, 120–137. [[CrossRef](#)]
10. Meinert, L.D.; Dipple, G.M.; Nicolescu, S. World skarn deposits. In *Economic Geology 100th Anniversary Volume 2005*; Society of Economic Geologists, Inc.: Littleton, CO, USA, 2005; pp. 299–336.
11. Liu, B.; Kong, H.; Wu, Q.H.; Chen, S.F.; Li, H.; Xi, X.S.; Wu, J.H.; Jiang, H. Origin and evolution of W mineralization in the Tongshanling Cu-polymetallic ore field, South China: Constraints from scheelite microstructure, geochemistry, and Nd-O isotope evidence. *Ore Geol. Rev.* **2022**, *143*, 164764. [[CrossRef](#)]
12. Huang, X.D.; Lu, J.J.; Stanislas, S.; Wang, R.C.; Ma, D.S.; Zhang, R.Q. The genetic differences between Cu-Pb-Zn and W-bearing granites in the Middle-Late Jurassic of Nanling: Taking Tongshanling and Weijia deposits in southern Hunan as examples. *Sci. China Earth Sci.* **2017**, *47*, 766–782.
13. Cao, J.Y.; Yang, X.Y.; Du, J.G.; Wu, Q.H.; Kong, H.; Li, H.; Wan, Q.; Xi, X.S.; Gong, Y.S.; Zhao, H.R. Formation and geodynamic implication of the Early Yanshanian granites associated with W-Sn mineralization in the Nanling range, South China: An overview. *Int. Geol. Rev.* **2018**, *60*, 1744–1771. [[CrossRef](#)]
14. Qin, Z.W.; Fu, J.M.; Xing, G.F.; Cheng, S.B.; Lu, Y.Y.; Zhu, Y.X. Petrogenetic differences among the Middle-Late Jurassic W, Sn, Pb-Zn-Cu-bearing granites in the Nanling Range, South China. *Geol. China* **2021**, *49*, 518–541.
15. Guo, C.L.; Xu, Y.M.; Luo, F.S.; Zheng, J.J. A comparative study of the Middle Jurassic granodiorite related to Cu and the Late Jurassic granites related to Sn in the Qin-Hang metallogenic belt and a tentative discussion on their tectonic dynamic setting. *Acta Petrol. Et Mineral.* **2013**, *32*, 463–484. (In Chinese)
16. Zhou, X.M.; Sun, T.; Shen, W.Z.; Shu, L.S.; Niu, Y.L. Petrogenesis of Mesozoic granitoids and volcanic rocks in South China: A response to tectonic evolution. *Episodes* **2006**, *29*, 26–33. [[CrossRef](#)]
17. Mao, J.W.; Cheng, Y.B.; Chen, M.H.; Franco, P. Major types and time-space distribution of Mesozoic ore deposits in South China and their geodynamic settings. *Mineral. Depos.* **2013**, *48*, 267–294.
18. Barrie, C.T. U-Pb garnet and titanite age for the Bristol Township lamprophyre suite, western Abitibi Subprovince, Canada. *Can. J. Earth Sci.* **1990**, *27*, 1451–1456. [[CrossRef](#)]
19. Gevedon, M.; Semen, S.; Barnes, J.D.; Lacey, J.S.; Stockli, D.F. Unraveling histories of hydrothermal systems via U-Pb laser ablation dating of skarn garnet. *Earth Planet. Sci. Lett.* **2018**, *498*, 237–246. [[CrossRef](#)]
20. Jamtveit, B.; Wogelius, R.A.; Fraser, D.G. Zonation patterns of skarn garnets: Records of hydrothermal system evolution. *Geology* **1993**, *21*, 113. [[CrossRef](#)]
21. Yudinsev, S.V.; Lapina, M.I.; Ptashkin, A.G.; Ioudintseva, T.S.; Utsunomiya, S.; Wang, L.M.; Ewing, R.C. Accommodation of Uranium Into the Garnet structure. *MRS Online Proc. Libr. Arch.* **2002**, *713*, 1128. [[CrossRef](#)]
22. DeWolf, C.P.; Zeissler, C.J.; Halliday, A.N.; Mezger, K.; Essene, E.J. The role of inclusions in U-Pb and Sm-Nd garnet geochronology: Stepwise dissolution experiments and trace uranium mapping by fission track analysis. *Geochim. Cosmochim. Acta* **1996**, *60*, 121–134. [[CrossRef](#)]
23. Duan, Z.; Gleeson, S.A.; Gao, W.S.; Wang, F.Y.; Li, C.J.; Li, J.W. Garnet U-Pb dating of the Yinan Au-Cu skarn deposit, Luxi District, North China Craton: Implications for district-wide coeval Au-Cu and Fe skarn mineralization. *Ore Geol. Rev.* **2020**, *118*, 103–310. [[CrossRef](#)]
24. Mezger, K.; Hanson, G.; Bohlen, S. U-Pb systematics of garnet: Dating the growth of garnet in the Late Archean Pikwitonei granulite domain at Cauchon and Natawahunan Lakes, Manitoba, Canada. *Contrib. Mineral. Petrol.* **1989**, *101*, 136–148. [[CrossRef](#)]
25. Seman, S.; Stockli, D.F.; McLean, N.M. U-Pb geochronology of grossular-andradite garnet. *Chem. Geol.* **2017**, *460*, 106–116. [[CrossRef](#)]
26. Fu, Y.; Sun, X.M.; Li, D.F.; Lin, H. U-Pb geochronology and geochemistry of U-rich garnet from the giant Beiya gold-polymetallic deposit in SW China: Constraints on skarn mineralization process. *Minerals* **2018**, *8*, 128. [[CrossRef](#)]
27. Zhang, L.S.; Peng, J.T.; Lin, F.M. Mineralogical, geochemical characteristics and formation mechanism of skarn minerals in the Darongxi tungsten deposit, western Hunan. *Geol. Rev.* **2021**, *66*, 113–139.

28. Huang, X.D.; Lu, J.J.; Stanislas, S.; Wang, R.C.; Wu, J.W.; Ma, D.S. Reworked restite enclave: Petrographic and mineralogical constraints from the Tongshanling intrusion, Nanling Range, South China. *J. Asian Earth Sci.* **2018**, *166*, 1–18. [[CrossRef](#)]
29. Wei, D.F.; Bao, Z.Y.; Fu, J. Geochemical characteristics and zircon SHRIMP dating of Tongshanling granites in Hunan. *Geotecton. Miner.* **2007**, *31*, 482–489. (In Chinese)
30. Lu, Y.Y.; Fu, J.M.; Cheng, S.B.; Liu, S.S.; Li, C.B.; Zhang, L.G.; Ma, L.Y. Rock-Forming and Ore-Forming Ages of Tongshanling Copper Polymetallic Ore-Field in Southern Hunan Province. *Geotecton. Et Metallog.* **2015**, *39*, 1061–1071. (In Chinese)
31. Wang, Y.C.; Duan, D.F. REE distribution character in skarn garnet and its geological implication. *Acta Sci. Nat. Univ. Pekin.* **2021**, *57*, 446–458.
32. Chen, J.; Jahn, B.M. Crustal evolution of southeastern China: Nd and Sr isotopic evidence. *Tectonophysics* **1998**, *284*, 101–133. [[CrossRef](#)]
33. Li, Z.X.; Li, X.H.; Zhou, H.; Kinny, P.D. Grenvillian continental collision in south China: New SHRIMP U-Pb zircon results and implications for the configuration of Rodinia. *Geology* **2002**, *30*, 163–166. [[CrossRef](#)]
34. Zhang, C.L.; Santosh, M.; Zou, H.B.; Li, H.K.; Huang, W.C. The Fuchuan ophiolite in Jiangnan Orogen: Geochemistry, zircon U-Pb geochronology, Hf isotope and implications for the Neoproterozoic assembly of South China. *Lithos* **2013**, *179*, 263–274. [[CrossRef](#)]
35. Shu, L.S.; Zhou, X.M.; Deng, P. Geological features and tectonic evolution of Meso-Cenozoic basins in Southeastern China. *Geol. Bull. China* **2004**, *23*, 876–884. (In Chinese)
36. Mao, J.W.; Xie, G.Q.; Guo, C.L.; Chen, Y.C. Large-scale W-Sn mineralization in the Nanling region, South China: Metallogenic ages and corresponding geodynamic process. *Acta Petrol. Sin.* **2007**, *23*, 2329–2338. (In Chinese)
37. Li, W.S.; Ni, P.; Wang, G.G.; Yang, Y.L.; Pan, J.Y.; Wang, X.L.; Chen, L.L.; Fan, M.S. A possible linkage between highly fractionated granitoids and associated W-T mineralization in the Mesozoic Yaogangxian granitic intrusion, Nanling region, South China. *J. Asian Earth Sci.* **2020**, *193*, 104314. [[CrossRef](#)]
38. Yang, J.H.; Peng, J.T.; Zheng, Y.F.; Hu, R.Z.; Bi, X.W.; Zhao, J.H.; Huang, J.C.; Zhang, B.L. Petrogenesis of the Mesozoic Shuikoushan peraluminous I-type granodioritic intrusion in Hunan Province, South China: Middle-lower crustal reworking in an extensional tectonic setting. *J. Asian Earth Sci.* **2016**, *123*, 224–242. [[CrossRef](#)]
39. Yang, J.H.; Kang, L.F.; Peng, J.T.; Zhong, H.; Gao, J.F.; Liu, L. In-situ elemental and isotopic compositions of apatite and zircon from the Shuikoushan and Xihuashan granitic plutons: Implication for Jurassic granitoid-related Cu-Pb-Zn and W mineralization in the Nanling Range, South China. *Ore Geol. Rev.* **2018**, *93*, 382–403. [[CrossRef](#)]
40. Wang, Y.F.; Yang, H.M.; Zhang, L.G.; Lu, S.S.; Yang, Z.F.; Qiu, X.F.; Liu, Z.P. Metallogenic epoch and ore-forming material source of the Tongshanling Pb-Zn polymetallic deposit in southeastern Hu'nan province: Evidence from Sm-Nd isochron age and Pb isotope. *Geol. Soc. Am. Bull.* **2017**, *36*, 875–884. (In Chinese)
41. Peng, J.T.; Hu, R.Z.; Yuan, S.D.; Bi, X.W.; Shen, N.P. The time ranges of granitoid Emplacement and related nonferrous metallic mineralization in southern Hunan. *Geol. Rev.* **2008**, *54*, 617–625. (In Chinese)
42. Ding, T.; Ma, D.; Lu, J.; Zhang, R. Apatite in granitoids related to polymetallic mineral deposits in southeastern Hunan Province, Shi-Hang zone, China: Implications for petrogenesis and metallogenesis. *Ore Geol. Rev.* **2015**, *69*, 104–117. [[CrossRef](#)]
43. Zong, K.Q.; Klemd, R.; Yuan, Y.; He, Z.Y.; Guo, J.L.; Shi, X.L.; Liu, Y.S.; Hu, Z.C.; Zhang, Z.M. The assembly of Rodinia: The correlation of early Neoproterozoic (ca. 900 Ma) high-grade metamorphism and continental arc formation in the southern Beishan Orogen, southern Central Asian Orogenic Belt (CAOB). *Precambrian Res.* **2017**, *290*, 32–48. [[CrossRef](#)]
44. Hu, Z.C.; Zhang, W.; Liu, Y.S.; Gao, S.; Li, M.; Zong, K.Q.; Chen, H.H.; Hu, S.H. “Wave” Signal-Smoothing and Mercury-Removing Device for Laser Ablation Quadrupole and Multiple Collector ICPMS Analysis: Application to Lead Isotope Analysis. *Anal. Chem.* **2015**, *87*, 1152–1157. [[CrossRef](#)]
45. Liu, Y.S.; Hu, Z.C.; Gao, S.; Günther, D.; Xu, J.; Gao, C.G.; Chen, H.H. In situ analysis of major and trace elements of anhydrous minerals by LA-ICP-MS without applying an internal standard. *Chem. Geol.* **2008**, *257*, 34–43. [[CrossRef](#)]
46. Meffre, S.; Large, R.R.; Scott, R.; Woodhead, J.; Chang, Z.; Gilbert, S.E.; Danyushevsky, L.V.; Maslennikov, V.; Hergt, J.M. Age and pyrite Pb-isotopic composition of the giant Sukhoi Log sediment-hosted gold deposit, Russia. *Geochim. Et Cosmochim. Acta* **2008**, *72*, 2377–2391. [[CrossRef](#)]
47. Chew, D.M.; Petrus, J.A.; Kamber, B.S. U-Pb LA-ICP-MS dating using accessory mineral standards with variable common Pb. *Chem. Geol.* **2014**, *363*, 185–199. [[CrossRef](#)]
48. Bodnar, R.J. Revised equation and table for determining the freezing point depression of H₂O-NaCl solutions. *Geochim. Et Cosmochim. Acta* **1993**, *57*, 683–684. [[CrossRef](#)]
49. Sun, S.S.; McDonough, W.F. Chemical and isotopic systematics of oceanic basalts: Implications for mantle composition and processes. *Geol. Soc. Lond. Spec. Publ.* **1989**, *42*, 313–345. [[CrossRef](#)]
50. Smith, M.; Henderson, C. The rare earth elements and uranium in garnets from the Beinn an Dubhaich Aureole, Skye, Scotland, UK: Constraints on processes in a dynamic hydrothermal system. *Petrol* **2004**, *45*, 457–484. [[CrossRef](#)]
51. Gaspar, M.; Knaack, C.; Meinert, L.D.; Moretti, R. REE in skarn systems: A LA-ICP-MS study of garnets from the Crown Jewel gold deposit. *Geochim. Et Cosmochim. Acta* **2008**, *72*, 185–205. [[CrossRef](#)]
52. Menzer, G. Die Kristallstruktur von Granat. *Z. Für Krist.* **1926**, *63*, 157–158.
53. McIntire, W.L. Trace element partition coefficients—A review of theory and applications to geology. *Geochim. Et Cosmochim. Acta* **1963**, *27*, 1209–1264. [[CrossRef](#)]

54. Carlson, W.D. Rates and mechanism of Y, REE, and Cr diffusion in garnet. *Am. Mineral.* **2012**, *97*, 1598–1618. [[CrossRef](#)]
55. Park, C.; Song, Y.; Kang, I.M.; Shim, J.; Chung, D.; Park, C.S. Metasomatic changes during periodic fluid flux recorded in grandite garnet from the Weondong W-skarn deposit, South Korea. *Chem. Geol.* **2017**, *451*, 135–153. [[CrossRef](#)]
56. Peng, H.J.; Zhang, C.Q.; Mao, J.W.; Santosh, M.; Zhou, Y.M.; Hou, L. Garnets in porphyry–skarn systems: A LA-ICP-MS, fluid inclusion, and stable isotope study of garnets from the Hongniu-Hongshan copper deposit, Zhongdian area, NW Yunnan Province, China. *J. Asian Earth Sci.* **2015**, *103*, 229–251. [[CrossRef](#)]
57. Quartieri, S.; Antonioli, G.; Geiger, C.A.; Artioli, G.; Lottici, P.P. XAFS characterization of the structural site of Yb in synthetic pyrope and grossular garnets. *Phys. Chem. Miner.* **1999**, *26*, 251–256. [[CrossRef](#)]
58. Quartieri, S.; Chaboy, J.; Antonioli, G.; Geiger, C.A. XAFS characterization of the structural site of Yb in synthetic pyrope and grossular garnets. II: XANES full multiple scattering calculations at the Yb L_I- and L_{III}-edges. *Phys. Chem. Miner.* **1999**, *27*, 88–94. [[CrossRef](#)]
59. Zhang, Y.; Shao, Y.J.; Zhang, R.Q.; Li, D.F.; Liu, Z.F.; Chen, H.Y. Dating ore deposit using garnet U-Pb geochronology: Example from the Xinqiao Cu-S-Fe-Au deposit. *East. China. Miner.* **2018**, *8*, 31. [[CrossRef](#)]
60. Li, D.F.; Tan, C.Y.; Miao, F.Y.; Liu, Q.F.; Zhang, Y.; Sun, X.M. Initiation of Zn-Pb mineralization in the Pingbao Pb-Zn skarn district, South China: Constraints from U-Pb dating of grossular-rich garnet. *Ore Geol. Rev.* **2019**, *107*, 587–599. [[CrossRef](#)]
61. Dziggel, A.; Wulff, K.; Kolb, J.; Meyer, F.M.; Lahaye, Y. Significance of oscillatory and bell-shaped growth zoning in hydrothermal garnet: Evidence from the Navachab gold deposit, Namibia. *Chem. Geol.* **2009**, *262*, 262–276. [[CrossRef](#)]
62. Tian, Z.D.; Leng, C.B.; Zhang, X.C.; Zafar, T.; Zhang, L.J.; Hong, W.; Lai, C.K. Chemical composition, genesis and exploration implication of garnet from the Hongshan Cu-Mo skarn deposit SW China. *Ore Geol. Rev.* **2019**, *112*, 103016. [[CrossRef](#)]
63. Jiang, Y.H.; Jiang, S.Y.; Dai, B.Z. Middle to late Jurassic felsic and mafic magmatism in southern Hunan province, southeast China: Implications for a continental arc to rifting. *Lithos* **2009**, *107*, 185–204. [[CrossRef](#)]
64. Wang, Y.J.; Fan, W.M.; Guo, F.; Li, H.M.; Liang, X.Q. U-Pb dating of Mesozoic granodioritic intrusions in southeastern Hunan Province and its petrogenetic implication. *Sci. China Earth Sci.* **2001**, *45*, 271–280. (In Chinese)
65. Quan, T.J.; Wang, G.; Zhong, J.L.; Fei, L.D.; Kong, H.; Liu, S.J.; Zhao, Z.Q.; Guo, B.Y. Petrogenesis of granodiorite in Tongshanling mining area, Hunan: Litho-geochemistry, U-Pb chronology and Hf isotope constraints. *Rocks Miner.* **2013**, *33*, 43–52. (In Chinese)
66. Lu, Y.F.; Ma, L.Y.; Qu, W.J.; Mei, Y.P.; Chen, X.Q. U-Pb and Re-Os isotope geochronology of Baoshan Cu-Mo polymetallic ore deposit in Hunan province. *Acta Petrol. Sin.* **2006**, *22*, 2483–2492. (In Chinese)
67. Huang, J.C.; Peng, J.T.; Yang, J.H.; Zhang, B.L.; Xu, C.X. Precise zircon U-Pb and molybdenite Re-Os dating of the Shuikoushan granodiorite-related Pb-Zn mineralization, southern Hunan, South China. *Ore Geol. Rev.* **2015**, *71*, 305–317. [[CrossRef](#)]
68. Zhang, S.T.; Chen, H.Y.; Shu, Q.H.; Zhang, Y.; Chu, G.B.; Cheng, J.M.; Tian, J. Unveiling growth histories of multi-generational garnet in a single skarn deposit via newly-developed LA-ICP-MS U-Pb dating of grandite. *Gondwana Res.* **2019**, *73*, 65–76. [[CrossRef](#)]
69. Zhang, X.B.; Zhang, S.T.; Chen, H.Y.; Liu, J.A.; Cheng, J.M.; Chu, G.B.; Li, S.S. Garnet LA-ICP-MS U-Pb dating of the Gaoyishan Wo (-Cu) deposit (Southeast Hubei Province) and its geological significance. *Earth Sci.* **2020**, *45*, 856–868. (In Chinese)
70. Deng, X.D.; Li, J.W.; Luo, T.; Wang, H.Q. Dating magmatic and hydrothermal processes using andradite-rich garnet U-Pb geochronometry. *Contrib. Mineral. Petrol.* **2017**, *172*, 1–11. [[CrossRef](#)]
71. Fan, G.H.; Li, J.W.; Deng, X.D.; Gao, W.S.; Li, S.Y. Age and origin of the Dongping Au-Te deposit in the north China craton revisited: Evidence from paragenesis, geochemistry, and in situ U-Pb geochronology of garnet. *Econ. Geol.* **2020**, *166*. [[CrossRef](#)]
72. Goldstein, R.H.; Reynolds, T.J. Systematics of fluid inclusions in diagenetic minerals. *Soc. Econ. Paleontol. Mineral.* **1994**, *31*, 199.
73. Diamond, L.W. Systematics of H₂O inclusions. *Mineral. Assoc. Can. Short Course* **2003**, *32*, 55–79.
74. Bauer, M.E.; Burisch, M.; Ostendorf, J.; Krause, J.; Frenzel, M.; Seifert, T.; Gutzmer, J. Trace element geochemistry of sphalerite in contrasting hydrothermal fluid systems of the Freiberg district, Germany: Insights from LA-ICP-MS analysis, near-infrared light microthermometry of sphalerite-hosted fluid inclusions, and sulfur isotope geochemistry. *Miner. Depos.* **2019**, *54*, 237–262.
75. Wang, Y.F. Ore-Forming Timing and Material Source of the Tongshanling Pb-Zn-Cu Polymetallic Deposit in Southern Hunan Province. Master's Thesis, China University of Geosciences, Wuhan, China, 2017. (In Chinese).
76. Bau, M. Rare-earth element mobility during hydrothermal and metamorphic fluid-rock interaction and the significance of the oxidation state of europium. *Chem. Geol.* **1991**, *93*, 219–230. [[CrossRef](#)]
77. Zhang, Y.; Liu, Q.Q.; Shao, Y.J.; Li, H.B. Fingerprinting the hydrothermal fluid characteristics from LA-ICP-MS trace element geochemistry of garnet in the Yongping Cu deposit, SE China. *Minerals* **2017**, *7*, 199. [[CrossRef](#)]
78. Zhang, Y.; Shao, Y.J.; Wu, C.D.; Chen, H.Y. LA-ICP-MS trace element geochemistry of garnets: Constraints on hydrothermal fluid evolution and genesis of the Xinqiao Cu-S-Fe-Au deposit, eastern China. *Ore Geol. Rev.* **2017**, *86*, 426–439. [[CrossRef](#)]
79. Sverjensky, D.A. Europium redox equilibria in aqueous solution-ScienceDirect. *Earth Planet. Sci. Lett.* **1984**, *67*, 70–78. [[CrossRef](#)]
80. Putnis, A. Mineral Replacement Reactions. *Rev. Mineral. Geochem.* **2009**, *70*, 87–124. [[CrossRef](#)]
81. Tian, M.J.; Li, X.C.; Guo, J.H.; Li, Y.G.; Zhang, Y. Composition of garnet from the Yongping Cu skarn deposit, South China: Implication for ore-fluid evolution. *Ore Geol. Rev.* **2021**, *139*, 104585. [[CrossRef](#)]

Disclaimer/Publisher's Note: The statements, opinions and data contained in all publications are solely those of the individual author(s) and contributor(s) and not of MDPI and/or the editor(s). MDPI and/or the editor(s) disclaim responsibility for any injury to people or property resulting from any ideas, methods, instructions or products referred to in the content.